This is a non peer-reviewed preprint submitted to EarthArXiv.
This manuscript has been submitted to Quaternary Science reviews for peer review
Subsequent versions of this manuscript may have slightly different content. We welcome feedback. Please contact Rienk Smittenberg (rienk.smittenberg@geo.su.se) regarding this manuscript's content

A 18,000-year Record of Tropical Land Temperature, Convective Activity and Rainfall Seasonality from The Maritime Continent

Rienk H Smittenberg [1*], Kweku A Yamoah [1]†, Frederik Schenk [1,2], Akkaneewut Chabangborn [1]‡, Sakonvan Chawchai [1]‡, Minna Väliranta [3], Barbara Wohlfarth [1]

[1] Department of Geological Sciences and Bolin Centre for Climate Research, Stockholm University, Stockholm, Sweden.

[2] Rossby Centre, Swedish Meteorological and Hydrological Institute, 601 76 Norrköping, Sweden.

[3] Environmental Change Research Unit, Department of Environmental Sciences, University of Helsinki, Finland.

† now at School of Geography, University of Birmingham, Birmingham, UK.

‡ now at Department of Geology, Chulalongkorn University, Bangkok 10330, Thailand.

[*] Corresponding author: rienk.smittenberg@geo.su.se

Highlights

- First continuous, high resolution record of land temperature from the maritime continent
- Land temperatures of the maritime continent were *ca.* 5°C colder at the last glacial termination compared to today and *ca.* 2°C warmer during the mid-Holocene climate optimum
- Strong seasonality at the end of the last glacial until the early Holocene caused a savannah vegetation with regular biomass burning
- The strong seasonality greatly influenced dictating vegetation proxies like $\delta^{13}C_{wax}$, by influencing vegetation (C4 Savanna C4 vs C3 rainforest) and the mean annual water isotopic signal recorded as δD_{wax} and $\delta^{18}O$
- Orbitally forced 'Wet Season Insolation' is positively correlated with both mean annual tropical temperature and the intensity of deep atmospheric convection.
- Indication of megadroughts at the onset of the Meghalayan period

Keywords:
Maritime continent, leaf wax hydrogen isotopes, carbon isotopes, biomass burning, seasonality, paleotemperature, paleohydrology, Late Glacial, Holocene

Abstract

The maritime continent exports an enormous amount of heat and moisture to the rest of the globe via deep atmospheric convection. How this export has changed through time during over de Late Glacial period and through the Holocene is hardly known, yet critical for the understanding of global climate dynamics. In this study, we present a very well dated, continuous paleoclimatic and -environmental record from southern Thailand covering the last 18,000 years, including the first land-based temperature reconstruction of the maritime continent. Confirming a recent climate modelling study, we found evidence for a strongly seasonal climate for most of the late glacial period, causing biomass burning and suppression of rainforest growth, despite rising CO_2 levels and increasing mean humidity. Temperatures were *ca.* 5°C cooler than today during the last cold stadial periods, and *ca.* 2°C warmer between 7000-2000 yr ago. We also found that tropical wet-season insolation (WSI) is a primary driver of the strength of deep atmospheric convection, exerting a strong influence on the both the Monsoon systems and the Walker circulation, and hence on global climate dynamics.

1 Introduction

The maritime continent (MC) forms the central part of the Indo-Pacific Warm Pool (IPWP), defined as the equatorial region with sea surface temperatures (SST) above 28ºC. This region is also called the 'steam engine of the world'. It constitutes a critical component of the global climate system by providing large amounts of latent heat to the higher latitudes via deep atmospheric convection, particularly via the monsoon systems (De Deckker, 2016). The MC also forms a key node in the tropical Walker circulation above the Indian and Pacific Ocean, which is modulated by the El Niño-Southern Oscillation (ENSO) (Timmermann et al., 2018) and Indian Ocean Dipole (IOD) (Mohtadi et al., 2017). Changes in rainfall in the MC have large consequences for both society and ecosystems, where drought-induced biomass burning and peat oxidation can induce rapid release of large amounts of carbon to the atmosphere (e.g. Randerson et al., 2005). A major change in the MC over the last glacial-interglacial (G-I) transition was the inundation of formerly exposed Sundaland and the Sahul shelf north of Australia. It has long been recognized that the submergence of this vast tropical landmass – approximately the size of the Amazon basin - must have had substantial consequences for global-scale climate dynamics (Koutavas and Joanides, 2012; DiNezio and Tierney, 2013; Di Nezio et al., 2016; Mohtadi et al., 2017; Yamoah et al., 2021). Palynological data from the former North Sunda and Molengraaff rivers and their deltaic deposits indicate that the region was covered with lowland rainforest that included sedges, reeds, bamboo, palms and ferns, suggesting fairly humid conditions throughout the last glacial maximum (LGM) around Borneo (Sun Xiang Jun and Sun Xiang Jun, 2002; Wang et al., 2009). In contrast, other proxy records from the region indicate drier conditions during the LGM (DiNezio and Tierney, 2013; Dubois et al., 2014). Highest ('driest') $\delta^{18}O$ values are recorded in a Borneo speleothem record at that time (Partin et al., 2007), and evidence exists for forest contraction and generally drier conditions in both peninsular Malaysia and Palawan during the LGM suggesting the existence of a savannah corridor (Heaney, 1991; Wurster et al., 2010; Wurster et al., 2019). A viable explanation lies in rainfall seasonality, which can strongly impact proxy records of both vegetation and the recorded water isotope signal. A recent climate modelling study (Hällberg et al., 2022) found that the tropical SE Asian climate was strongly seasonal during the Late glacial, with very arid conditions during the northern Hemisphere winter period. The seasonal aridity was driven by orbital forcing and stronger East Asian winter monsoon caused by a much larger latitudinal temperature gradient than today. A breakdown of deep convection during NH winters caused a reorganized Walker Circulation and a mean state resembling El Niño conditions. Spatial coverage of high-resolution paleoclimate records from this vast region remains scant, however, which is partially explained by the fact that much of Sundaland has disappeared under the waves. Insight into the spatial patterns and mechanisms of the, sometimes rapid, climatic changes that occurred during the G-I transition, as well as over the Holocene, is therefore still limited for this climatically important region. In this study we present a high-resolution, very well dated (Fig. S1) and continuous 18,000 year-long multi-proxy record from lake Nong Thale Prong (NTP, 8˚17´N, 99˚37´E) located in southern Thailand at the northwestern border of former Sundaland (Fig. 1).

Lake NTP is a shallow (<7 m water depth), small (~210 m^2) karst lake at ~60 m above sea level (Snansieng et al., 1976). More details of the lake setting can be found in an earlier publication (Yamoah et al., 2016) that focused on the ecological evolution over the last 150 years using ancient DNA and lipid biomarkers. We used the stable carbon isotopic composition of leaf wax-derived long-chain *n*-alkanes ($\delta^{13}C_{wax}$) as a proxy for the relative abundance of C3 vs. C4 vegetation, which is influenced by pCO_2, temperature and seasonality (Dubois et al., 2014; Pinto et al., 2014). This data set was combined with the stable hydrogen isotope composition of the same leaf wax alkanes (δD_{wax}) and charcoal to gain further information about hydroclimate (Sachse et al., 2012) and seasonality. We also present the first high-resolution land-based temperature record of the MC, based on bacterial-derived branched glycerol dialkyl glycerol tetraethers (brGDGTs) (Sun et al., 2011; Schouten et al., 2013; Russell et al., 2018). The combined proxy records reveal how the aerial exposure and subsequent inundation of Sundaland interacted with orbital and other climate forcings to impact the hydroclimate of SE Asia.

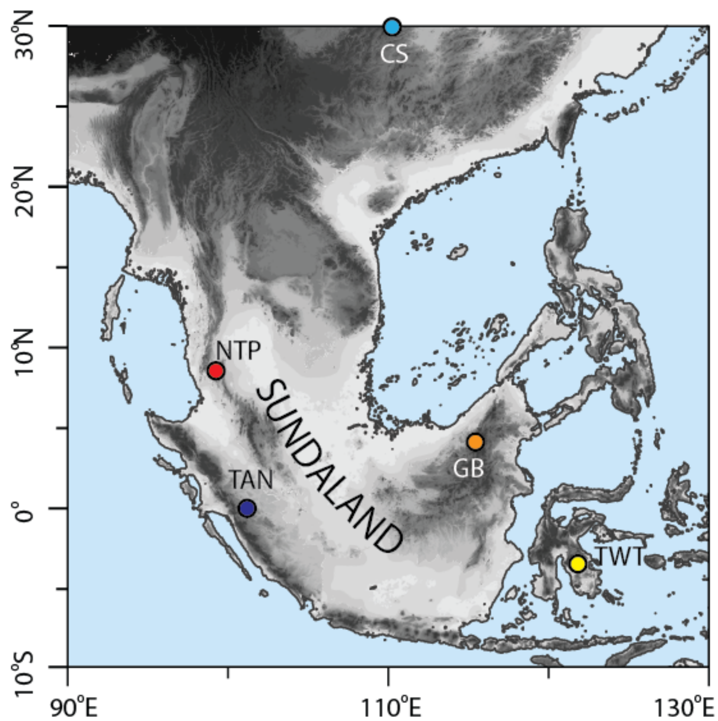

Fig. 1. Location of Lake Nong Thale Prong (NTP) and other records mentioned in the text. GB: Gunung Buda National Park speleothem, Borneo; TWT: Lake Towuti, Sulawesi; CS: Chinese Speleothems; TAN: Tangga cave, Sumatra. The map shows the extent of the emerged landscapes of former Sundaland during the last glacial maximum sea level low stand.

2. Materials and Methods

2.1 Sampling and sample processing

Two parallel sediment cores were retrieved in one-meter sections using a rod-operated Russian corer from a small raft at the deepest part of the lake. After recovery, the sections were wrapped in foil and secured and transported in PVC tubes to Stockholm University, where they were stored at 4°C until further description (Table S1) and analysis. Sub-samples were taken in contiguous 1-cm increments and split to accommodate subsequent analyses. One half of the samples was utilized for macrofossil and charcoal analysis and radiocarbon dating. The other half of the samples was freeze-dried and analysed for loss-on-ignition (LOI), bulk total organic carbon (TOC), nitrogen (TN) and their bulk isotopes (Table S4), lipid biomarkers and compound-specific hydrogen and carbon isotopes. For LOI, samples were dried overnight at 105°C, ground and then combusted at 550 °C for 3h. LOI was calculated as a percentage of the dry sample weight to obtain an estimate of the organic matter and carbonate content. In parallel, a sediment-water interface surface core covering the last 150 years was retrieved and sampled on site in one cm slices (Yamoah et al., 2016).

2.2 Macrofossil analysis and radiocarbon dating

Approximately 380 samples were sieved under running water (mesh sizes 0.5 and 0.25 mm) to recover plant macrofossils for radiocarbon dating. Plant remains were picked with tweezers under a binocular microscope, described, and rinsed multiple times in deionized water, placed in pre-cleaned glass vials and dried overnight at 105 °C. 59 samples were dated at the 14Chrono Centre, Queen's University Belfast, where pre-treatment and measurement followed the methodology described in (Chawchai et al., 2015). Based on these, an age-model (Fig. S1) was constructed using Bacon, a Bayesian statistics-based routine (Blaauw and Christen, 2011) that estimates the accumulation rate for sediment segments based on the radiocarbon dates calibrated using the intCal13 NH calibration curve (Reimer et al., 2013). Radiocarbon dates are given in Table S2.

2.3 Bulk geochemistry

%TOC, %TN and bulk $\delta^{13}C_{org}$ and bulk $\delta^{15}N_{bulk}$ were measured on a Carlo Erba NC2500 elemental analyser, coupled to a Finnigan MAT Delta^{+} mass spectrometer. To remove carbonates, samples were fumigated with HCl within a dessicator prior to analysis. $\delta^{13}C_{bulk}$ is expressed in ‰ against the Vienna PeeDee Belemnite (VPDB) standard, and had an analytical error of less than ±0.15‰. $\delta^{15}N_{bulk}$ are reported in ‰ relative to air (N), with an analytical error of ±0.15‰. Results are listed in Table S3.

2.4 Lipid biomarkers

Lipid extraction was performed on freeze-dried samples by sonication with a mixture of dichloromethane and methanol (DCM-MeOH 9:1 v/v) for 20 minutes and subsequent centrifugation. The process was repeated three times and supernatants were combined. Aliphatic hydrocarbon fractions were isolated from the total lipid extract using silica gel columns (5% deactivated) that were first eluted with pure hexane (F1) and subsequently with a mixture of DCM-MeOH (1:1 v/v) to obtain a polar fraction (F2). A saturated hydrocarbon fraction was obtained by eluting the F1 fraction through 10% $AgNO_3$ impregnated silica gel using pure hexane as eluent. The saturated hydrocarbon fractions were analyzed by gas chromatography – mass spectrometry for identification and quantification, using a Shimadzu GCMS-QP2010 Ultra. C_{21} to C_{33} *n*-alkanes were identified based on mass spectra from the literature and retention times. The concentrations of individual compounds were determined using a calibration curve made using mixtures of C_{21}-C_{40} alkanes of known concentration and used to optimize the concentrations for compound-specific isotope analysis.

2.5 Leaf wax hydrogen and carbon isotope analysis

The hydrogen isotopic composition of *n*-alkanes (expressed in delta notation in ‰ against VSMOW) was analyzed by gas chromatography–isotope ratio monitoring–mass spectrometry (GC-IRMS) using a Thermo Finnigan Delta V mass spectrometer interfaced with a Thermo Trace GC 2000 using the HTC reactor of a GC Isolink II and Conflo IV system. Helium was used as a carrier gas at constant flow mode and the compounds separated on a Zebron ZB-5HT Inferno GC column (30 m x 0.25 mm x 0.25μm). A standard set of alkanes with known isotopic composition (obtained from A. Schimmelmann, Indiana University, USA) was used for daily calibration of the reference gas. The average standard deviation of δD values was 5‰. The reported δD_{wax} values are the average of the most abundant long chain *n*-alkanes: C_{27}, C_{29} and C_{31}. To correct for the higher global average of global oceanic δD during lower sea levels, the δD values of the *n*-alkanes were ice volume corrected (*c.f.* Tierney and deMenocal, 2013) as follows: $\delta D_{wax\text{-}c} = (\delta D_{wax} + 1000) / (\delta O^{18}{}_{w} * 8 * 0.001 + 1) - 1000$, with interpolated ocean water $\delta O^{18}{}_{w}$ values (Waelbroeck et al., 2002). $\delta^{13}C_{wax}$ was measured on the same compounds on the same system and the same isotope standards, except for the use of the combustion reactor. $\delta^{13}C_{wax}$ values are the average of C_{27}, C_{29} and C_{31} alkanes, expressed in delta notation in ‰ against VPDB, with an average standard deviation of 0.5‰. Results are presented in tables S5 (leaf wax δD) and S6 (leaf wax $\delta^{13}C$).

2.6 Glycerol dialkyl glycerol tetraether (GDGT) analysis

Branched glycerol dialkyl glycerol tetraethers (brGDGTs) were measured on the F2 fractions after reconstituting in MeOH:DCM 9:1 and subsequent filtration through 0.45 μm PTFE filters, following published protocols (Rattray and Smittenberg, 2020). Analysis was done using a Thermo-Dionex HPLC connected to a Thermo Scientific TSQ quantum access triple quadrupole mass spectrometer, using an APCI interface. Chromatographic separation was achieved on a Kinetex C18-XB reverse phase column using a gradient of mobile phase A: MeOH with 0.04% formic acid and mobile phase B: propan-2-ol with 0.04% formic acid. GDGTs were detected in SIM mode at *m/z* 1020 (scan width 7, 0.2s), 1034 (width 7, 0.2s), 1048 (width 7, 0.2s), 1296 (width 17.5, 0.5s). Quantification was performed using Excalibur software, using the (M+) and (M+1) ions of the GDGTs. More details can be found elsewhere (Rattray and Smittenberg, 2020). MBT and CBT proxies were calculated following Weijers et al. (2007). GDGT results and reconstructed MAAT are presented in table S7.

A basic prerequisite for the valid use of brGDGTs is a relatively high branched-over-isoprenoid tetraether (BIT) index, which was 1.0 throughout the core. Reconstructed pH values, based on the CBT index (Weijers et al., 2007) were 8.0±0.2 over the entire core, with lowest values during the

Younger Dryas and a downward trend for the last 2000 years (Fig. S4). This means that temperature is the dominant environmental factor exerted on the brGDGT distribution, and that confounding factors like changes in setting (e.g., between peat/wetland and lake) and pH (De Jonge et al., 2021) are likely minimal. At the time of measurement, we had not adopted the new HILIC-based method which separates between 5-methyl and 6-methyl branched GDGTs (Hopmans et al., 2016) but used our own method based on reverse phase chromatography (Rattray and Smittenberg, 2020), similar to the one used by (Zhu et al., 2013), and which compared well with the original method using a cyano column. As a consequence, we do not have individual quantifications of 5-methyl and 6-methyl branched GDGT isomers used in the revised MBT'_{5me} temperature proxy for mineral soils (De Jonge et al., 2014), peats (Naafs et al., 2017), or East African lakes (Russell et al., 2018). However, for high temperatures as is the case for our site, the main response to temperature is a shift between tetra- and pentamethylated GDGTs, which makes the differentiation between 5- and 6-methyl GDGTs less relevant compared to colder environments.

3 Results

3.1 Proxy validation

The relative abundance of tetra-, penta- and hexamethylated GDGTs plot in the same region as datasets produced with the HILIC method from east African lakes and from global soils and peats (Fig S4). This strengthens the confidence that the brGDGTs we measured can be used as a temperature proxy. Among the various GDGT-temperature calibrations that have been developed since the original one (Weijers et al., 2007), we chose to apply the global lake calibration of Sun et al. (2011) for lakes with pH<8.5, which also included data from nearby lake Towuti:

$$MAAT_{Sun\text{-}cal} = 3.949 + 38.213\ MBT - 5.593\ CBT \qquad \text{(Eq. 1)}$$

We performed a present-day proxy evaluation and calibration by comparing proxy data analyzed from the surface sediments with instrumental data for the last century. The MBT/CBT-based MAAT (°C) reconstruction using the global regression model of Sun et al. (2011) shows a good agreement with temperature observations in the region (closest grid point at 8.25° N; 99.25° E from the University of East Anglia Climate Research Unit dataset CRU TS3.23) (Harris et al., 2014) for the overlapping period of 1903-2001. There is however an offset and overestimation of variability in the proxy reconstruction using the global lake calibration relative to the local temperature. To adjust the reconstruction to our local conditions, we re-calibrated the global reconstruction by replacing the mean of the $MAAT_{Sun\text{-}cal}$ values obtained using the global regression ($\mu_{proxy\text{-}global}$) and standard deviation ($\sigma_{proxy\text{-}global}$) with those of local conditions from CRU TS3.23. This was done by first normalizing the proxy record for the overlapping period 1903-2001 and then re-normalize it using the mean ($\mu_{obs\text{-}local}$) and standard deviation ($\sigma_{obs\text{-}local}$) of the local observations for the same time period (Eq. 2).

$$MAAT_{i,local} = \left[(x_{i,proxy-global} - \mu_{Proxy-global}) \frac{\sigma_{Obs-local}}{\sigma_{Proxy-global}} \right] + \mu_{Obs-local} \qquad \text{(Eq. 2)}$$

resulting in a record of recalibrated $MAAT_{RC}$ values. This re-calibration effectively adjusts the intercept and slope of the original calibration so that the proxy data reflects the mean and annual variability observed over the instrumental record. Generating a new calibration by regression of the GDGT data with the instrumental record is not straightforward, because the samples do not correspond to annual measurements but approximately 3 years, with an error of the age estimate based on ^{210}Pb dating that increases with depth.

We even performed the same exercise using the original calibration (Weijers et al., 2007), and came to the same results (Fig. S4a). It is important to note that all data come from one location where the microbial ecology of the brGDGT-producing organisms and the dominant environmental factors vary much less compared to the globally distributed surface sediment datasets used to generate the GDGT calibrations. For reference, the RMSE of the East African lake calibration (Russell et al., 2018) is approximately 2.5°C.

δD_{wax} of the surface core (Yamoah et al., 2016)(table S8) closely follows the annual precipitation amount (Fig. 2a), where a 10‰ decrease in δD_{wax} corresponds to a 25% reduction in rainfall. This confirms earlier work relating convective activity with both greater rainfall and isotopic fractionation (the 'amount effect', e.g. (Bony et al., 2008) assuming that δD_{wax} predominantly reflects δD_{precip} after biosynthetic fractionation. Previous research has shown that the hydrogen isotopic composition of both terrestrial and aquatic biomarkers generally reflects that of their source water, although with an offset primarily due to biosynthetic fractionation effects (Sachse et al., 2012, 2004; Sessions et al., 1999). In the humid tropics, the fractionation ($\varepsilon_{wax/water}$) was found to be fairly constant at 130‰ (Feakins et al., 2016). Using this fractionation factor, back-calculated δD values for precipitation of the last century ranges between -40‰ and -60‰, reflecting actual measurements for the region (Wei et al., 2018).

$MAAT_{RC}$ and δD_{wax} correlate strongly with each other (Fig. 2c), and have the same relation to each other as observed during the seasonal cycle: clear skies during the drier seasons and years with less convective rainfall allow for higher surface temperatures, whereas high clouds associated with deep convection result in a cooling of the surface due to reflection (albedo) and atmospheric absorption of shortwave radiation (Sobel et al., 2010), an effect that is particularly strong in monsoonal Asia (Jalihal et al., 2019).

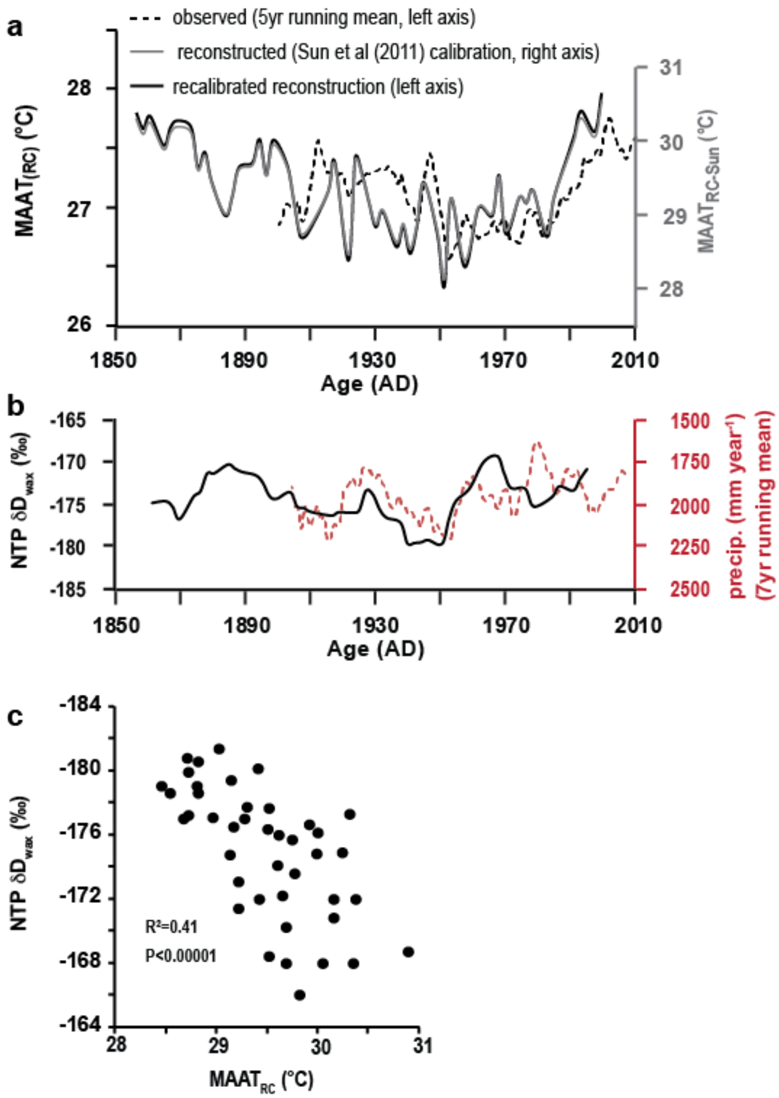

Fig. 2. Comparison of instrumental climate data with proxy data measured on the NTP surface sediments. a) Mean Annual Air Temperature ($MAAT_{RC\text{-}Sun}$) reconstructed using bacterial-derived branched GDGTs (right axis, grey), compared to observations (left axis, stippled black). To obtain a local calibration the reconstructed MAAT was scaled for amplitude and mean to correspond with the instrumental record (black, left axis). b) Instrumental rainfall data (right axis, stippled red) compared with δD_{wax} data from the same samples (Yamoah et al., 2016) suggests a good correlation between the two. c) Scatter plot of dD_{wax} and reconstructed MAAT from the same samples. Instrumental climate data are taken from the CRU TS monthly high-resolution gridded multivariate climate dataset, Version 4 (Harris et al., 2020).

3.2 Sedimentology and limnology

The 18,000 year-long lake NTP sequence consist of organic rich gyttja with TOC contents ranging between 10-40% (Fig. S2). TOC contents vary stepwise between 10 and 40% during the Late Glacial part of the core, high TOC contents between 9.5-4.2 ka BP, turning to somewhat lower and more variable contents over the last few millennia. Besides some variation caused by changes in minerogenic input, we interpret the TOC changes as mainly caused by alternations between meromictic conditions with permanent bottom water anoxia - leading to preservation of organic matter, and monomictic conditions - resulting in greater organic matter oxidation within the sediments. Stratification in tropical lakes is sensitive to small changes in the lake water level between wet and dry seasons, heat budgets and climate (e.g., wind stress), and other limnological or even ecological feedbacks (Lewis Jr, 1996). Given this multitude of factors, we do not attempt to interpret the TOC content. Notably, there is no correlation between the variable TOC content and the lipid biomarker proxies presented further below. This indicates that lake stratification and preservation of organic matter did not influence the primary climatic signal of our proxy records.

The continuous occurrence of seeds of the aquatic plant taxon *Najas* (Fig. 3f; SI Table 4, Fig. S2) and a robust age model showing no large changes in accumulation rate indicates that the shallow lake never dried out. *Cyperaceae* spp. remains, mostly seeds, also occur continuously throughout the sequence, except for the last few millennia when they are nearly absent.

The lower part of the sequence, deposited during Heinrich Stadial 1 (HS1, 18-14.7 ka BP), contains unidentified terrestrial plant remains including woody material, often co-occurring with charred plant remains and macroscopic charcoal; this was also the case for the Younger Dryas period (YD 12.8-11.5 ka BP). Charcoal was most abundant during HS1, then declined towards the end of the Late Glacial period, with irregular occurrences until the early Holocene around 9 ka BP. Ostracods shells are abundant throughout the HS1, leading to high carbonate contents, and this declines during the Bølling (Bø 14.7-14.0 ka).

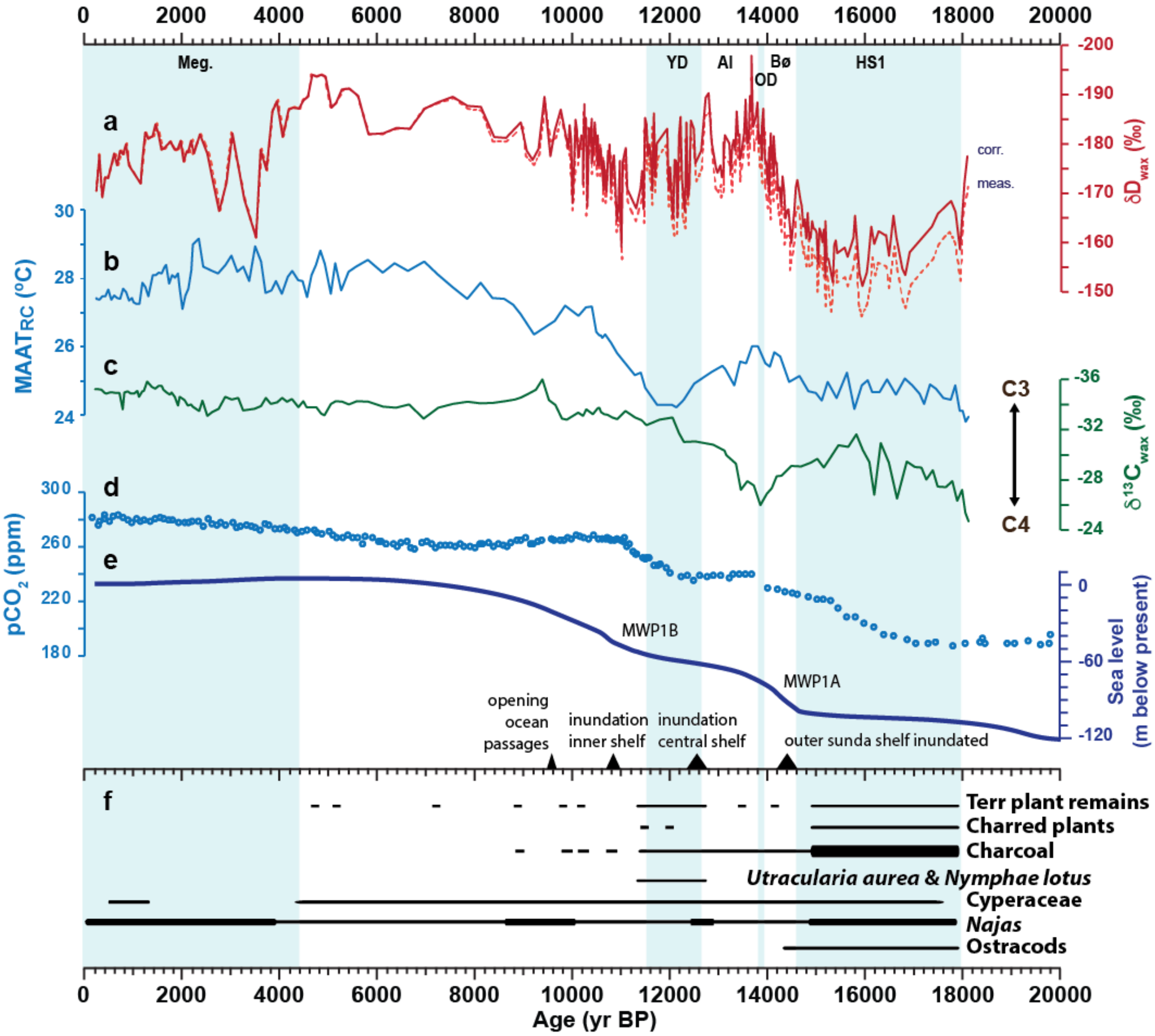

Fig. 3. Proxy records of lake NTP of the last 18,000 years. a) δD_{wax}, both as measured and corrected (stippled) for global sea level change. **b)** Reconstructed mean annual air temperature ($MAAT_{RC}$). **c)** $\delta^{13}C_{wax}$. **d)** Atmospheric CO_2 levels (Monnin, 2006). **e)** Sea level reconstruction for the Sunda Shelf region (Hanebuth et al., 2011) **f)** Macrofossil and charcoal results. Thick line: very abundant; Thin line: present.
Meg: Meghalayan period; YD: Younger Dryas; Al: Allerød; OD: Older Dryas; Bø:Bølling; HS1: Heinrich Stadial 1.
MWP: Meltwater pulses.

3.3 Temperature reconstruction

$MAAT_{RC}$ (Fig. 3b) stays around 23-24°C during HS1, a 5°C cooling compared to the present. This is more than the most recent estimate for the tropical ocean during the LGM (−4.2 to −3.7°C; (Tierney et al., 2020) but is in line with estimates based on tropical glacier snow line elevations (Porter, 2000). Temperatures rose during the Bø to reach a maximum of 26°C soon after the Older Dryas event (OD 14.0-13.8 ka BP), but declined during the Allerød (Al, 13.8-12.8 ka BP) and again reached stadial values at the end of the YD. With the start of the Holocene temperatures rose steadily to reach 28-29°C between 7-2 ka BP. The last two millennia are characterized by a cooling trend to a present-day $MAAT_{RC}$ of around 27°C.

3.4 $\delta^{13}C_{wax}$ as combined proxy for pCO_2, temperature and rainfall seasonality

Stable carbon isotope ($\delta^{13}C$) values of both of the long-chain *n*-alkanes ($\delta^{13}C_{wax}$) (Fig. 3c) and the bulk (Fig. S2) reflects a change from a landscape dominated by C4 grasses and sedges at the beginning of the record, to a humid tropical ecosystem dominated by ^{13}C-depleted C3 vegetation – likely forest - during the Holocene (*cf.* Garcin et al., 2014). The $\delta^{13}C$ record broadly follows the evolution of atmospheric CO_2 (Fig. 3d). This lends support to the hypothesis that low CO_2 concentration favored C4 vegetation during the LGM (Ehleringer et al., 1997; Collatz et al., 1998; Pinto et al., 2014). Our observation compares well to tropical African records (Street-Perrott, 1997; Cerling et al., 1998; Sinninghe Damsté et al., 2011). Increasing fractionation against ^{13}C at higher pCO_2 levels and greater humidity (Diefendorf and Freimuth, 2017; Hare et al., 2018) – regardless of plant type, can explain part of the trend. An exception to the general trend of increasingly more negative $\delta^{13}C$ from the LGM through the Holocene is a large excursion that starts at 16.0 ka BP, reaching the lowest $\delta^{13}C$ values at 13.8 ka BP.

3.5 δD_{wax} as proxy for precipitation

To further investigate past precipitation changes, we analyzed δD_{wax}, with higher resolution between 17-10 ka BP, to discern trends during deglaciation (Fig. 3a). δD_{wax} was corrected for the effect of global ice volume (Tierney and deMenocal, 2013). A confounding factor in the interpretation of δD_{wax} is the potential effect of changing vegetation and associated change in fractionation (Liu and Yang, 2008). For instance, C3 and C4 plant types tend to fractionate differently against deuterium and may moreover respond differently to drought in order to minimize water loss while still allowing gas exchange through the stomata (Wang et al., 2013; Garcin et al., 2014). The generally stronger biosynthetic fractionation against deuterium of C3 plants compared to C4 would however lead to an opposite behavior of δD_{wax} as observed: the increase in C4 during the Bølling period is associated with more negative δD_{wax}, not more positive. The same argument can be made from a possible transition from a grassy to more woody vegetation during the G-I transition, which would be expected to lead to less negative δD_{wax} values (Liu and Yang, 2008), but again the opposite is observed. From the perspective of vegetation change, our δD_{wax} record might thus even underestimate the original variations in source water δD.

4. Discussion

4.1 Late Glacial climate evolution

4.1.1 Inferences from $\delta^{13}C$

The unusual $\delta^{13}C$ excursion that starts at 16.0 ka BP suggests a renewed contribution of C4 vegetation to the carbon pool in this interval, even though the excursion is coincident with continued warming and its onset correlates with a change in the rate of increase in atmospheric pCO_2 (Fig. 3). The behavior of the $\delta^{13}C$ record indicates that the tropical lowland ecosystem of Sundaland represented an ecotone inhabiting the C3/C4 crossover line during the Late Glacial period. This ecosystem was sensitive to the antagonistic effects of rising pCO_2 and rising temperature on C3 versus C4 plants, where higher temperatures and/or lower pCO_2 favor C4 plants. However, a third important climatic factor also favors non-perennial C4 vegetation: rainfall seasonality (Dubois et al., 2014). Seasonal dryness was likely promoted by the presence of Sundaland, which only became fully inundated around 11 ka BP during Meltwater Pulse 1b (Hanebuth et al., 2011). This large landmass prevented the dry northern winds of the Asian winter monsoon from picking up moisture over the Sunda Sea as they do today. This effect was probably promoted by orbital forcing: insolation during NH winter declined while summer insolation increased between the LGM and the end early Holocene, favoring the strength of both the winter and summer monsoon. Strong seasonality promotes biomass production during the wet season, which then serves as fuel for biomass burning during a longer dry season (Murphy and Bowman, 2007). This severely limits the establishment of perennial C3 forests that would otherwise outcompete non-perennial C4 vegetation as atmospheric CO_2 levels rose. The charcoal record (Fig. 3f, SI Table 4) provides evidence that fires were a persistent feature during the entire Late Glacial period, especially during HS1. We therefore conclude that the return towards a larger contribution of C4 vegetation after 16 ka BP arose from a combination of rising temperatures with the continued rainfall seasonality, thereby offsetting the C3-promoting effect of increasing pCO_2. Our interpretation of strong seasonality concurs with CESM1 climate model simulation results that focused on the Late glacial period (Hällberg et al., 2022), which indicate that a large part of island SE Asia, apart from Borneo, experienced not only much reduced total rainfall compared to today, but especially a dry season lasting several months during NH winters. The trend toward increasing C4 (savannah) vegetation reversed after 13.8 ka BP, coinciding with highest $MAAT_{RC}$ and one of the fastest increases of pCO_2. Hällberg et al. (2022) found a strong seasonality for both 13 ka BP (i.e., Al) and 12 ka BP (i.e., YD) so gradual return to an increasing contribution of C3 (forest) vegetation was likely driven by the cooling trend that started already during the Al, supported by a further rise in pCO_2 during the YD. It is also possible that the local area started to experience a lesser rainfall seasonality, and/or higher general humidity, due to the ongoing inundation of Sundaland resulting in an ever more maritime climate despite the continuation of strong and dry winter monsoons until the start of the Holocene. The general trend in $\delta^{13}C$ observed at NTP also is evident in the lower resolution IPWP record from Lake Towuti on Sulawesi (Russell et al., 2014)(Fig. S3), supporting the interpretation of the combined influence of pCO_2 and rainfall seasonality over the entire IPWP over glacial-interglacial timescales.

4.1.2 Inferences from δD_{wax}

Starting at 18 ka BP, the δD_{wax} record increases to reach highest (least negative) values around 16 ka BP (Fig. 3), indicating that the driest conditions with the weakest convection and greatest evapotranspiration (Douglas et al., 2012) occurred during HS1, culminating at Heinrich Event 1. This is followed by a rapid decrease during the Bø, and, similar to the $MAAT_{RC}$ and $\delta^{13}C$ records, and subsequent a sharp reversal at the start of the Al. δD_{wax}, $MAAT_{RC}$ and $\delta^{13}C$ track each other until the YD, with lower δD_{wax} accompanying higher $MAAT_{RC}$, suggesting warmer and wetter conditions, and vice versa. This is consistent with inferences from the $\delta^{13}C$ record of patterns of change in C4 vegetation. The combined records suggest that the period of high rainfall seasonality may have had wetter wet seasons. However, climate model simulations (Hällberg et al., 2022) indicate generally dryer conditions even during the NH summer, besides strong NH droughts.

To explain the steep change in δD_{wax} between 16 and 14 ka BP, despite NH winter dryness, the convective strength over Sundaland must have increased, caused by rising temperatures during the Bø. Large-scale convective activity and rainfall amount are the dominant factors that influence water isotope values in tropical SE Asia, in addition to changes in moisture source region (Wei et al., 2018). Today, during NH summer (JJA), most moisture in southern Thailand is derived from the Indian Ocean, but during the wettest autumn season (SON) there is also a contribution from the South China Sea. In the past, however, moisture derived from evapotranspiration over Sundaland likely also contributed to the isotopic signature. At that time, longer air mass trajectories over land would have caused a larger rainout effect, leading to lower water isotope values similar to those of present-day mainland SE Asia (Wei et al., 2018). Lastly, the lower values might have been exacerbated by the seasonality of rainfall, because the final isotopic signal of water available for plant growth is biased towards that of the wet season (with lowest δD_{precip}) because of its larger contribution to the weighted annual mean.

4.1.3 Inferences from the combined δD_{wax}, $\delta^{13}C$, and $MAAT_{RC}$ records

The rapid sea level rise during MWP1a changed the hydrologic gradient and reduced the flow of Sundaland river systems. Together with monsoon intensification this most likely transformed the entire Sundaland region into a vast expanse of tropical wetlands (De Deckker, 2016) with abundant moisture and isotope recycling comparable to the present-day Amazon basin. The parallel reversal of δD_{wax}, $\delta^{13}C$ and $MAAT_{RC}$ around 13.8 ka BP, coincident with the OD event (Fig. 3), indicates a system change towards decreasing rainfall seasonality and a more marine climate. Higher year-round moisture availability would result in a greater contribution of less-depleted δD_{prec} during the cooler winter monsoon months, thereby raising annual mean δD. Lowering of MAAT can occur because of an increase in latent heat production and hence evaporative cooling throughout the year, at the expense of sensible heat. It is also possible that the cold winter monsoon had already started to strengthen during the Al period in response to a southward movement of the mean position of the intertropical convergence zone (ITCZ) caused by NH cooling, something that continued until the end of the YD (~11.5 ka BP). The hypothesis of a southward ITCZ is supported by the coherent patterns in the variability of δD_{wax} during the YD and the Greenland ice core $\delta^{18}O$ record, with shifts in the mean position of the ITCZ in response to latitudinal temperature gradients (Yuan et al., 2018). After the YD, however, δD_{wax} continues to increase until 11 ka BP, in opposition to the rapid change in the Greenland record, but interestingly enough also opposite to the local $MAAT_{RC}$. We attribute this to the development of a more equable hydroclimate throughout the year, with an increased relative contribution of 'dry'-season rainfall with higher δD values, sourced from the Gulf of Thailand and the South China Sea.

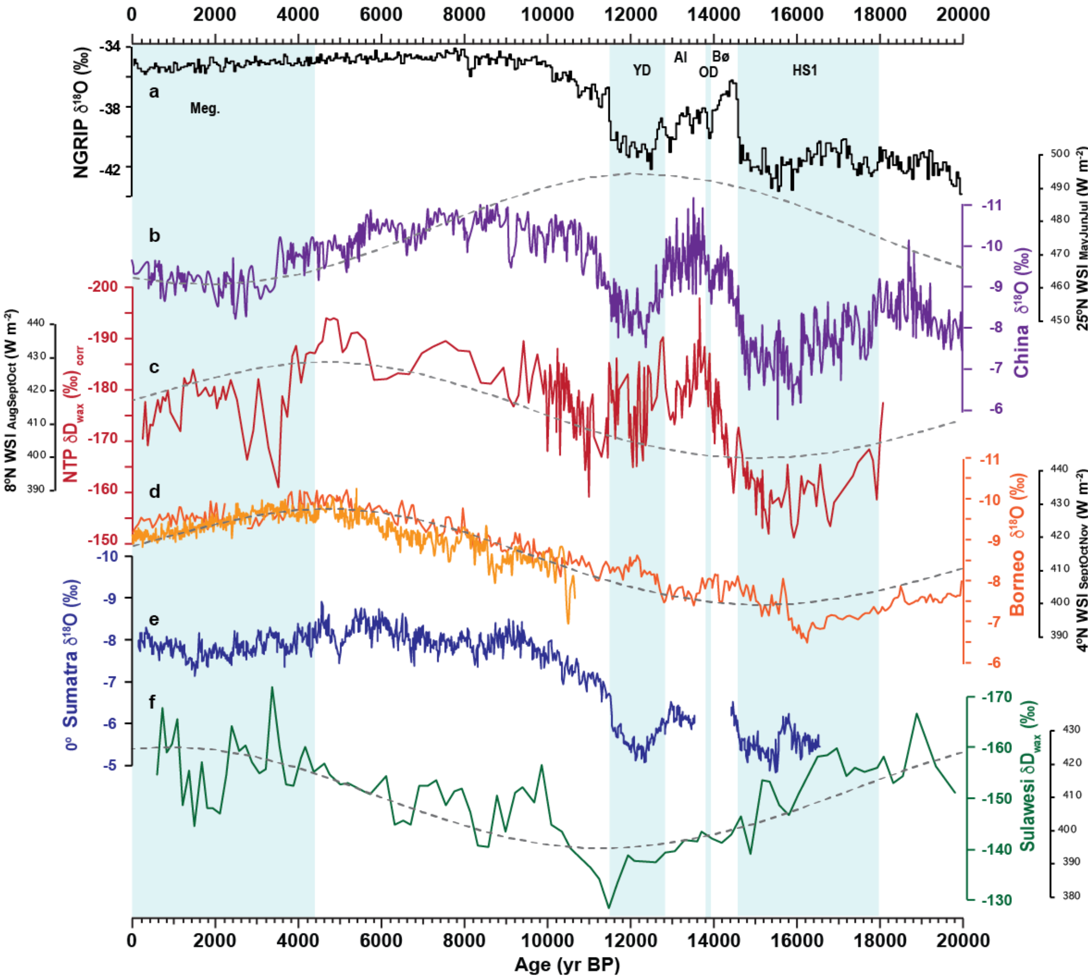

Fig. 4. Comparison of isotope records. **a**) Greenland ice core δ^{18}O as a reference for NH temperature (Andersen et al., 2004). **b**) Combined Chinese speleothem d^{18}O (Cheng et al., 2016). **c**) NTP δD_{wax} corrected for sea level effect (this study). **d**) Borneo speleothem δ ^{18}O record (dark, (Partin et al., 2007) and light (Chen et al., 2016), orange). **e**) Sumatra speleothem δ^{18}O record (Wurtzel et al., 2018). **f**) Sulawesi δD_{wax} record (Konecky et al., 2016). b-f are all plotted on the same scale where one unit in d ^{18}O corresponds to 8 units in d D space, according to the global meteoric water line. Grey dotted lines over b-d and f show the solar irradiation averaged for the 2 or 3 wettest months (WSI: Wet Season Insolation) for the latitudes of the respective records (Laskar et al., 2004). No clear wettest period could be defined for Sumatra. Time periods are shown as in in Figure 3.

4.2 Orbital forcing of Holocene and Late Glacial climate, and seasonality effects

4.2.1 Wet Season Insolation

After 11 kyr BP, δD_{wax} and $MAAT_{RC}$ vary again in tandem. Both show a generally asymptotic trend towards the warmest and wettest conditions peaking at ~4.5 ka BP. This indicates that the 'steam engine of the world', the IPWP, was at full power during the mid-Holocene thermal maximum, exporting greatest amounts of latent heat, i.e. moisture, to the Northern Hemisphere during this time. This long-term coupling between δD and $MAAT_{RC}$ at orbital to millennial scales is opposite to that of higher frequency relationships at annual to decadal scales (Fig. 2), where the total insolation is distributed between latent and sensible heat. Orbital-scale changes in the seasonal distribution of insolation apparently steer $MAAT_{RC}$ and convective strength in the same direction. The precessional cycle has indeed long been identified as the dominant component of orbital forcing influencing tropical and monsoonal climate (Clement et al., 1999; Jalihal et al., 2019). NH summer insolation (JJA) is most commonly used to explain the waxing and waning of monsoon strength, even though leads and lags between proxy records exist. In the tropics, however, the season of most intense rainfall does not occur during JJA. Thus, we compare our records with 'wet season' insolation (WSI), i.e., the mean monthly insolation during the wettest part of the annual cycle at 8ºN. Indeed, δD_{wax} follows the insolation curve for the wettest months, September-November (Fig. 4) (Laskar et al., 2004), although with a notable excursion during the Bø/Al-YD periods, which we attribute to the influence of increasing seasonality combined with a much stronger (cold) Asian Winter monsoon under Late glacial conditions when the higher latitudes were still significantly colder than today, as discussed above.

The 7% variation of WSI over the last 18,000 years (418 - 446 kW/m^2) (Laskar et al., 2004) thus appears to be a main driver of both surface (temperature) and atmospheric (latent, convective) heat flux. This observation is consistent with a Borneo (4ºN) speleothem record (Chen et al., 2016), where $\delta^{18}O$ is correlated with the wettest months at that latitude (Fig. 4). The δD_{wax} record from Lake Towuti (Sulawesi) has been interpreted as being driven primarily by changes in moisture source and air trajectories (Konecky et al., 2016), but it also shows a strong correspondence with WSI at 2ºS (Dec&Jan, during the passing of the ITCZ; Fig. 4). Both δD_{wax} records (NTP and Towuti) show a sensitivity to WSI of -1.4‰ per W/m^2, as does the Borneo record when scaled by a factor of eight for $\delta^{18}O$ according to the global meteoric water line. Combined, these records provide further evidence for the influence of the precessional cycle on the isotopic composition of regional precipitation, via the combined mechanisms of regional convective activity and associated amount of precipitation. This is exacerbated by secondary effects of seasonality, which also affects the distribution between latent and sensible heat. In the tropics there is a clear correlation between insolation and rainfall amount (Fig. S7), with at present lowest values in June and July (Fig. 5) (Wurtzel et al., 2018). Over the course of a precessional cycle, the shift in seasonal distribution of solar energy can be as much as 15%, which must be causing a large effect on seasonality. At and near the equator, the 'dry' season may even have shifted from NH summer to SH summer (Fig. 5), and the wettest season more towards or away from the March and September annual maximums, depending on the orbital phase. Because of this we did not assign a wet season insolation curve to the Tangga Cave record at Sumatra (Fig. 4).

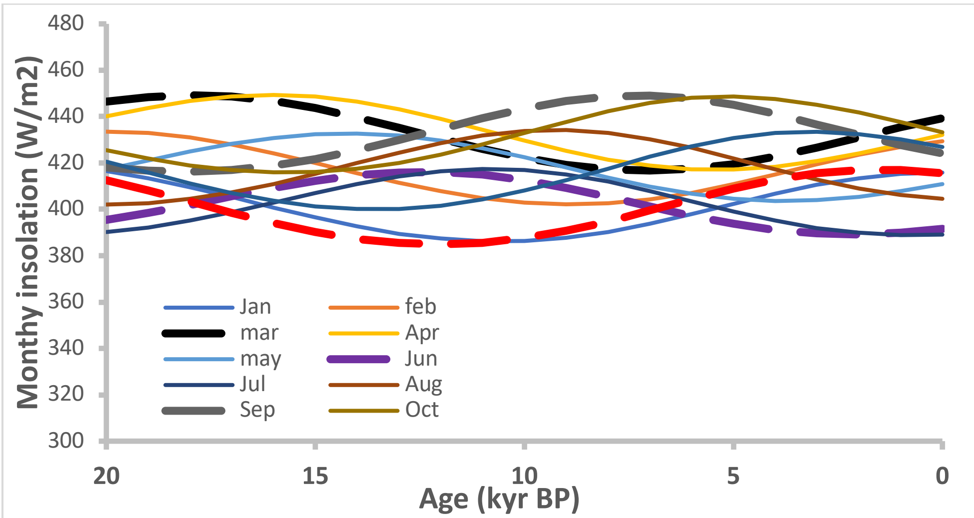

Figure 5. Monthly insolation curves for 0° (equator). Present-day (0 BP) June and July insolation are at their precessional low, and these months have correspondingly lowest rainfall amounts (compare with Wurtzel et al., 2018), while the months of December and January, with the same angle of the sun, have stronger insolation and greater rainfall (See Fig S7). Assuming a dominant influence of insolation on convective activity, the annual precipitation patterns likely change over the course of the precessional cycle.

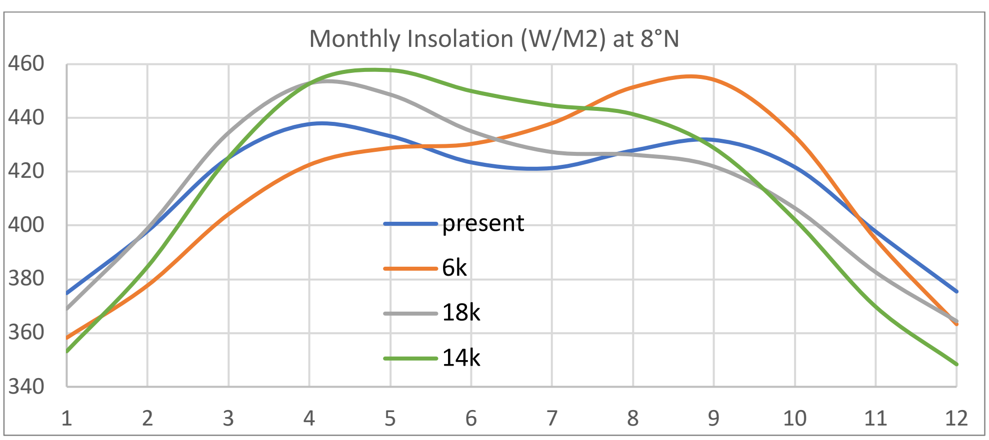

Fig. 6. Annual insolation curves at 8°N over selected periods from the last 18,000 years (Laskar et al., 2004) clearly showing the two maximums in April and August/September. Months are in numbers.

4.2.2. Relation between WSI and mean annual temperature water isotopes

At our site lake Nong Thale Prong at 8°N, the present-day annual insolation curve exhibits two highs: one in April and one in August/September (Fig. 6), when the sun's altitude is 90° at noon. The annual movement of the ITCZ and the Monsoon system behaves in an attenuated fashion (Fig. S5). From January onwards, temperatures rise (Fig. S6) but precipitation remains low until May,

because the ITCZ remains south. Dry conditions with low cloud cover cause low albedo, resulting in highest surface temperatures in April (Fig. S6). The ITCZ passes over quickly going northwards during May and June, to merge with the Asian Summer Monsoon system during the NH summer (Fig. S5). The Monsoon/ITCZ moves back towards the equator in NH autumn, causing the strongest period of convective precipitation over the northern IPWP from September-November (Figs. S5 and S6). During this time, much of the incoming radiation is reflected by high convective clouds, or is used to generate latent heat, leading to reduced surface temperatures (Fig. S6).
Between 6-4 ka BP, perihelium (the moment the earth is closest to the sun during its elliptical orbit) occurred in September-October, causing 5% greater insolation in September compared to today (Fig. 6). This stronger WSI for the SE Asian Monsoon and the northern IPWP will have caused warmer ocean surfaces and subsequently greater evaporation and convective activity both in the northern Indian Ocean (specifically the Bay of Bengal), as well as the South China sea. All this explains that lowest δD_{wax} values are observed in the mid Holocene. On top of that, precipitation was likely lower in spring with low insolation levels (Figs. 7 and Fig S5), causing a stronger bias of autumn rainfall towards the annual mean.

Higher mid Holocene MAATs result from a combination of drier and sunnier spring months, compensating for relatively low insolation levels (more sensible heat, less latent heat), and cloudy wet months that however receive highest solar inputs. Our data are thus consistent with the theory that the precessional cycle caused greater seasonality in the mid Holocene, compared to the low-seasonality period we currently experience. We discuss the interaction between precession and the annual cycle and its influence on precipitation seasonality and the mean annual isotope signal, together with MAAT, in further detail below.

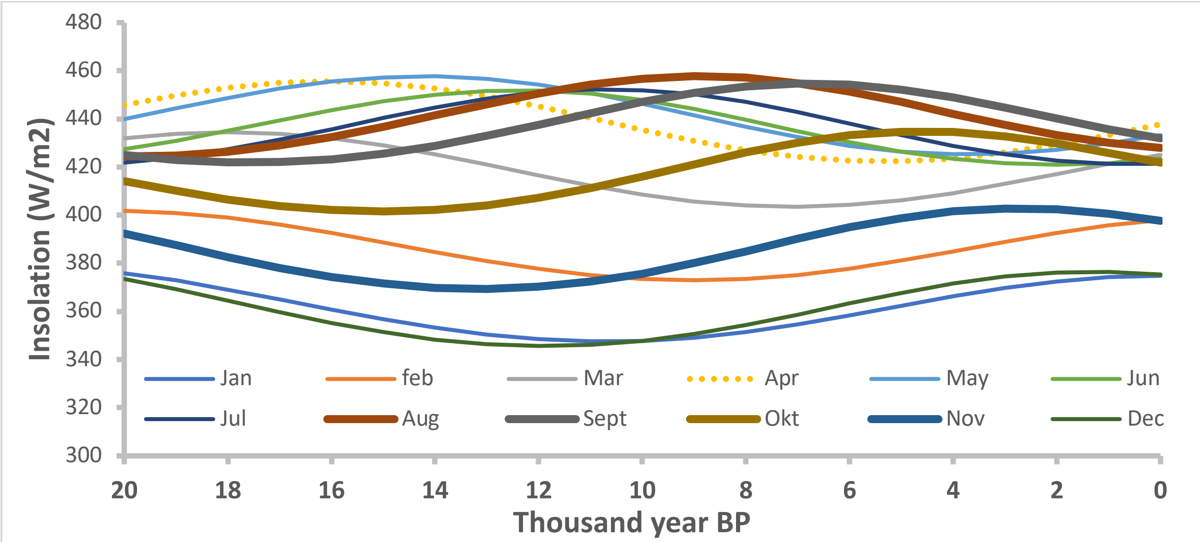

Figure 7. Mean monthly insolation (W/m^2) over the last 20,000 years for 8°N (Laskar et al., 2004), showing the waxing and waning of insolation energy over the precessional cycle for the various months. Insolation maximizes between 6-4 kyr BP for the wettest period SON (See Fig. S6). The insolation curves have the same shape for higher latitudes, but have different absolute values. The mainland SE Asian summer monsoon peaks in JAS, with highest insolation between 10-8 kyr BP and very low insolation at the present. Note that the age axis is reverse compared to proxy records.

Looking further back at 20 kyr BP, the seasonal pattern of insolation is similar as today (Fig. 7), but over the ensuing Late Glacial period (i.e., towards 14 ka BP) perihelion shifts towards NH spring. Being a mirror case of the situation at 6 ka BP, this would cause higher convective activity in the northern IPWP during spring with moisture sourced from the Pacific side. In NH autumn, the lower insolation would have caused a weakened ITCZ convection. Different to today, however, was the presence of Sundaland. Air masses coming from the northeast would not have been able to pick up as much moisture as they can today over South China Sea. Consequently, the greater NH spring insolation only could lead to more rainfall when Sundaland became a large wetland, allowing more land surface evapotranspiration. Until then, the annual sum of precipitation would have derived almost exclusively from the autumn. After 14 ka BP, the perihelion moves towards NH summer, and insolation remains high from spring through summer and into the autumn. After 12 ka BP, insolation becomes ever more focused on the autumn (all autumn months go 'up'; Fig. 7), until 6 ka BP, thus aligning ever more with the annual movement of the ITCZ and the period of strongest convection. Over the last millenniums, perihelium has shifted from NH winter towards spring.

The relative strength of insolation and related convective activity distributed over the year will have had its effect on the annual weighted mean of δD of precipitation. Results for nearby Phuket (Wei et al., 2018) indicate only a relatively small range in $\delta^{18}O$ through the year, from -2‰ (i.e. δD = -7‰) in April to -8‰ (δD = -55‰) in November, with an annual weighted average of -5.5‰ (δD = -35‰). The moment a shorter season is responsible for the majority of the annual sum, i.e., when the perihelion aligns with the wettest months in autumn, then the weighted mean annual isotope value will shift towards that season. This is the likely situation in the mid Holocene around 6 ka BP where isotopically relatively heavy spring precipitation would have contributed less to the annual mean, while the stronger convective activity during the wet autumn season would have caused more depleted wet season precipitation. Together, this causes a bias towards lower mean annual δD values at times of strong seasonality. This seasonal bias also means that there does not need to be any close relation between total annual rainfall and the mean isotopic composition. The seasonal bias on the mean annual isotopic composition is likely a factor that has influenced other isotope records from the tropics as well, instead of being solely caused by changes in rainfall amount or moisture source.

4.3 Relation of IPWP climate with the Asian monsoon system and ENSO

4.3.1 Export and attenuation of 'peak isotope' in SE Asia

Lastly, we discuss the effect of the precessional cycle on advected moisture. In the early Holocene, perihelion (i.e., highest insolation) occurred during the start of the Asian summer monsoon, when the advected moisture in mainland SE Asia does not yet reach very depleted values ($\delta^{18}O$ = -18‰ (Wei et al., 2018)). In the mid-late Holocene, however, perihelion has shifted to the autumn, at a time when the moisture reaching mainland SE Asia is already much more depleted. The expected shift of the Monsoon strength towards the autumn will thus also cause a shift in the mean isotope composition - even if at the local scale insolation and therefore total monsoon strength has already decreased. The end result is an attenuation of 'peak isotope', because of the source effect, and not because of the amount effect. This effect can explain the temporal shift of 'peak isotope' away from the time perihelium occurred during classical NH summer (JJA, between 10-8 ka BP) towards later (8-6 ka BP) as observed in the Chinese speleothem records.

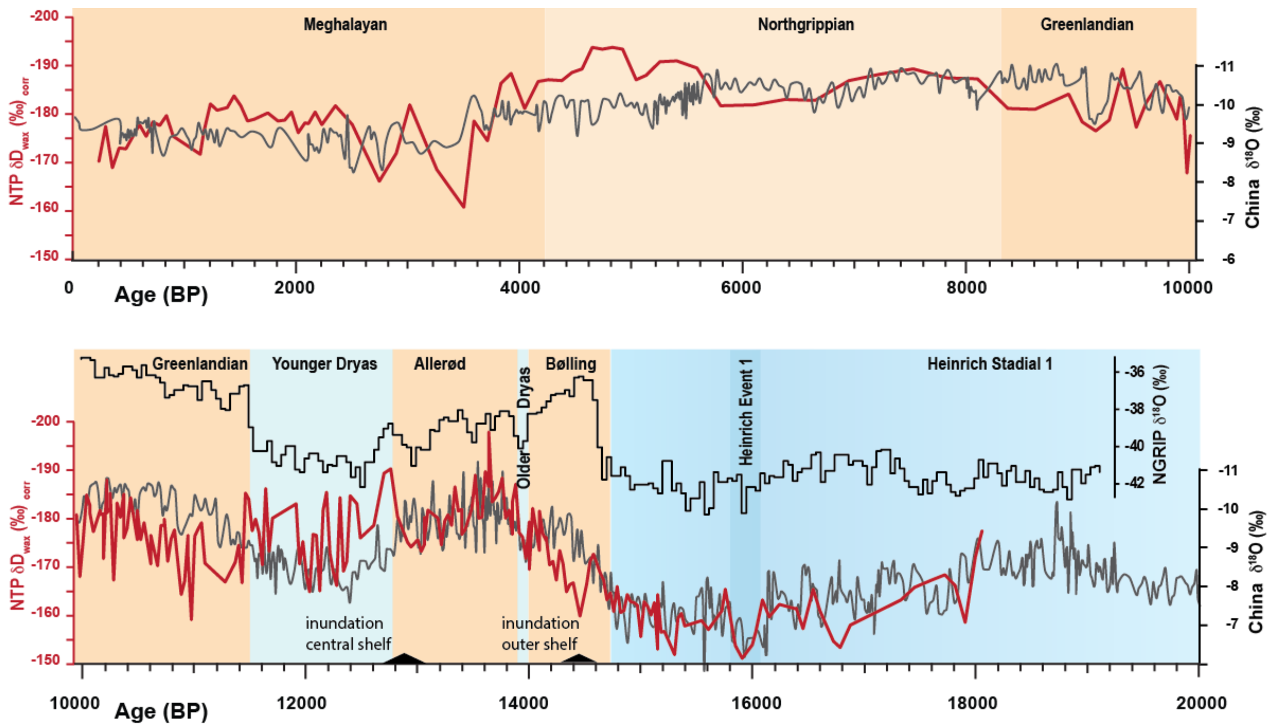

Fig. 8. Comparison of the NTP δD_{wax} (this study) with the Chinese speleothem $\delta^{18}O$ records (Cheng et al., 2016). Both records resemble each other very well, including a number of short-term events like Heinrich Event 1. For reference, the Late Glacial Greenland $\delta^{18}O$ (Andersen et al., 2004) record is also plotted. The records are scaled in the same way as in Fig. 4.

4.3.2 Influence of IPWP hydroclimate on the Asian monsoon and ENSO

The trends in the NTP δD_{wax} record are similar to those in the Asian speleothem $\delta^{18}O$ records (Cheng et al., 2016; Zhang et al., 2019) (Fig. 8), including the OD event and the 'peak isotope' feature at the beginning of the Al. NTP δD_{wax} also tracks the Greenland ice core record (Fig. 8), reflecting the impact of high-latitude NH forcing on tropical climate. NTP receives most of its moisture from the Indian Ocean, in contrast to the East Asian speleothems, which also receive significant summer monsoon moisture from the East (Wei et al., 2018; Zhang et al., 2019). The shared patterns of variation are consistent with modeling studies (Yang et al., 2014; Pausata et al., 2011), which have shown that East Asian speleothem $\delta^{18}O$ records reflect the isotopic composition of the advected moisture, as much or more so than rainfall amount, and that large-scale convection patterns are the main drivers of the isotopic composition of precipitation (Wei et al., 2018). Our results, which are similar to those from a recent study in northern Thailand (Yamoah et al., 2021), demonstrate that the exposure and inundation of Sundaland played a critical role in affecting the water isotopic composition not only across mainland East Asia, but also in Thailand. Hällberg et al. (2022) found a complete breakdown of convection over former Sundaland during NH winter for Lateglacial conditions, resulting in an El-Niño-like mean state with extended dry seasons. They attribute this mainly to orbital forcing, combined with a still much colder NH hemisphere causing a much large temperature gradient between the tropics and the higher latitudes. The same factors that lowered δD_{wax} at our site (more rainout and more land-derived moisture from Sundaland, and greater seasonality), must also have applied further inland. Remote processes upstream of the SE Asian Monsoon, such as the presence / inundation of Sundaland, precession-forced changes in WSI in the lower tropics, and seasonality, need to be considered when interpretating SE Asian water isotope records in sediments and speleothems. Experiments with isotope-enabled general circulation models are needed to gain further insight.

4.4. Late Holocene droughts

Another last notable feature of the δD_{wax} record are the positive ('dry') excursions between 4 and 3 ka BP, which is coincident with the onset of the Meghalayan age (Fig. 3), characterized by megadroughts observed in multiple regions (Kathayat et al., 2018). The dry events occur on top of a general decline in convective activity, which follows the decrease in WSI after 5 ka BP. Our results of a wettest and warmest mid Holocene extend the recent finding (Dang et al., 2020) of a warmer mid Holocene thermocline in the IPWP east of 115°E, caused by greater September insolation. The warmer and deeper thermocline causes a stronger zonal thermal difference across the equatorial Pacific, which further promotes deep atmospheric convection and rainfall over western equatorial Pacific in a positive feedback mechanism, inducing a stronger Walker circulation and suppression of ENSO activity. This mechanism weakened when WSI in the northern IPWP lessened, which may have allowed the crossing of a climate tipping point allowing ever greater ENSO activity. The interaction of the precessional and seasonal cycles that act upon the IPWP, being the 'steam engine of the world', thus appears to play a decisive role in global climate dynamics by regulating the amount of latent heat exported to the higher latitudes and dictating the existence and strength of ENSO. In this respect, we even speculate that the inundation and warming of Sundaland and may have provided a key positive feedback mechanism during the last G-I transition, and possibly also earlier ones.

5. Conclusions

A main conclusion that can be drawn from our multi-proxy record is that seasonality is a major factor that needs to be taken into consideration when interpreting climate and vegetation proxies like $\delta^{13}C_{wax}$ and δD_{wax}. Our data show that over the Late Glacial period the aerially exposed Sundaland experienced a more continental and especially more seasonal climate than today with biomass burning during dry winters, favoring C4 (Savannah) vegetation. This feature is most apparent during the Bølling period that saw a rapid warming and strong increase in seasonal precipitation conditions. A key turning point in a tug-of-war between pCO_2, temperature and seasonality as the three driving factors determining the ratio of C3 and C4 vegetation was the Older Dryas event at 13.8 ka BP, after which climate evolved towards that of the year-round humid climate known from the present day. Our Holocene record shows a clear mid-Holocene optimum of deep convection in the northern IPWP, indicating that the 'steam engine of the world' was at full power exporting greater amounts of (latent) heat, i.e. moisture, to the Northern Hemisphere during this time. This declined over the last 5000 years, with dramatic effects starting in the Meghalayan age at 4.2 ka BP where we find some evidence of severe droughts. Inferred from our own and from other records, we argue that 'wet season' insolation (WSI), following the precessional cycle, predicts convective strength, rainfall amount and intensity, distilling into an isotope effect of -1.4‰ for δD (and -0.175‰ for $\delta^{18}O$) per W/m^2 for the WSI. It is this weighted mean isotope signal that gets predominantly recorded in water isotope-based proxies. Moreover, we observe a long-lasting coupling between the hydrological cycle and MAAT, where temperatures are driven by the cumulative effects of rainfall (cloud) seasonality imposed by the precessional cycle, even though mean annual insolation hardly changes. Our first, continuous record of mean annual terrestrial temperature from tropical SE Asia confirms earlier compiled evidence that tropical temperatures in the LGM were 4-5°C lower than today. The close resemblance of our record with other Asian speleothem $\delta^{18}O$ records indicates that the tropical SE Asian climate is dictated by the combined effects of the precessional cycle, seasonality, and the changing continentality of the IPWP region over glacial cycles due to sea level change. Our results highlight the importance of the IPWP as the 'steam engine of the world' to global climate, and how it responds to orbital forcing and sea level change.

Acknowledgments

We wish to thank Sherilyn Fritz, Wichuratree Klubseang and Sudo Inthonkaew for sampling assistance and discussion. Jayne Rattray and Anna Hägglund and Camilla Bredberg are thanked for laboratory assistance. Paula Reimer from Queen's University of Belfast conducted the radiocarbon analyses.

Funding This work was supported by Swedish Research Council (VR) research grants 621-2008-2855 (RHS), 348-2008-6071 (BW) and 621-2011-4916 (BW).

Author contributions

Conceptualization: RHS, BW

Sampling: BW, KAY, AC, SC

Analysis: BW, KAY, RHS, MV, SC

Supervision: RHS, BW

Writing : RHS

Commenting: BW, KYA, FS, MV, SC, AC

Competing interests: Authors declare that they have no competing interests.

Data and materials availability: The data presented in this paper is available online as csv files and as excel file at the Bolin Centre of Climate Research Database:
Barbara Wohlfarth, Rienk Smittenberg (2022) Temperature and hydrological data for the last 18,000 years from Lake Nong Thale Prong, Southern Thailand. Dataset version 1. Bolin Centre Database.
https://doi.org/10.17043/wohlfarth-2022-nong-thale-prong-1

Supplementary Materials

Figures S1-S7

Tables S1-S8 are available at the Bolin Center for Climate Research database:
https://doi.org/10.17043/wohlfarth-2022-nong-thale-prong-1

- Table 1. Composite stratigraphy
- Table 2. Radiocarbon data
- Table 3. Plant macrofossil and charcoal data
- Table 4. Bulk geochemistry: TOC, TN, LOI, bulk $\delta^{13}C$ and bulk $\delta^{15}N$
- Table 5. Leaf wax δD
- Table 6. Leaf wax $\delta^{13}C$
- Table 7. GDGTs and reconstructed MAAT
- Table 8. Surface Core GDGTs, reconstructed MAAT, leaf wax δD and instrumental MAAT

References

Andersen, K.K., Azuma, N., Barnola, J.-M., Bigler, M., Biscaye, P., Caillon, N., Chappellaz, J., Clausen, H.B., Dahl-Jensen, D., Fischer, H., Flückiger, J., Fritzsche, D., Fujii, Y., Goto-Azuma, K., Grønvold, K., Gundestrup, N.S., Hansson, M., Huber, C., Hvidberg, C.S., Johnsen, S.J., Jonsell, U., Jouzel, J., Kipfstuhl, S., Landais, A., Leuenberger, M., Lorrain, R., Masson-Delmotte, V., Miller, H., Motoyama, H., Narita, H., Popp, T., Rasmussen, S.O., Raynaud, D., Rothlisberger, R., Ruth, U., Samyn, D., Schwander, J., Shoji, H., Siggard-Andersen, M.-L., Steffensen, J.P., Stocker, T., Sveinbjörnsdóttir, A.E., Svensson, A., Takata, M., Tison, J.-L., Thorsteinsson, Th., Watanabe, O., Wilhelms, F., White, J.W.C., North Greenland Ice Core Project members, 2004. High-resolution record of Northern Hemisphere climate extending into the last interglacial period. Nature 431, 147–151. https://doi.org/10.1038/nature02805

Blaauw, M., Christen, J.A., 2011. Flexible paleoclimate age-depth models using an autoregressive gamma process. Bayesian Anal. 6, 457–474. https://doi.org/10.1214/11-BA618

Bony, S., Risi, C., Vimeux, F., 2008. Influence of convective processes on the isotopic composition (δ^{18} O and δ D) of precipitation and water vapor in the tropics: 1. Radiative-convective equilibrium and Tropical Ocean–Global Atmosphere–Coupled Ocean-Atmosphere Response Experiment (TOGA-COARE) simulations. J. Geophys. Res. 113, D19305. https://doi.org/10.1029/2008JD009942

Cerling, T.E., Ehleringer, J.R., Harris, J.M., 1998. Carbon dioxide starvation, the development of C4 ecosystems, and mammalian evolution. Phil. Trans. R. Soc. Lond. B 353, 159–171. https://doi.org/10.1098/rstb.1998.0198

Chawchai, S., Chabangborn, A., Fritz, S., Väliranta, M., Mörth, C.-M., Blaauw, M., Reimer, P.J., Krusic, P.J., Löwemark, L., Wohlfarth, B., 2015. Hydroclimatic shifts in northeast Thailand during the last two millennia – the record of Lake Pa Kho. Quaternary Science Reviews 111, 62–71. https://doi.org/10.1016/j.quascirev.2015.01.007

Chen, S., Hoffmann, S.S., Lund, D.C., Cobb, K.M., Emile-Geay, J., Adkins, J.F., 2016. A high-resolution speleothem record of western equatorial Pacific rainfall: Implications for Holocene ENSO evolution. Earth and Planetary Science Letters 442, 61–71. https://doi.org/10.1016/j.epsl.2016.02.050

Cheng, H., Edwards, R.L., Sinha, A., Spötl, C., Yi, L., Chen, S., Kelly, M., Kathayat, G., Wang, X., Li, X., Kong, X., Wang, Y., Ning, Y., Zhang, H., 2016. The Asian monsoon over the past 640,000 years and ice age terminations. Nature 534, 640–646. https://doi.org/10.1038/nature18591

Clement, A.C., Seager, R., Cane, M.A., 1999. Orbital controls on the El Niño/Southern Oscillation and the tropical climate. Paleoceanography 14, 441–456. https://doi.org/10.1029/1999PA900013

Collatz, G.J., Berry, J.A., Clark, J.S., 1998. Effects of climate and atmospheric CO 2 partial pressure on the global distribution of C 4 grasses: present, past, and future. Oecologia 114, 441–454. https://doi.org/10.1007/s004420050468

Dang, H., Jian, Z., Wang, Y., Mohtadi, M., Rosenthal, Y., Ye, L., Bassinot, F., Kuhnt, W., 2020. Pacific warm pool subsurface heat sequestration modulated Walker circulation and ENSO activity during the Holocene. Sci. Adv. 6, eabc0402. https://doi.org/10.1126/sciadv.abc0402

De Deckker, P., 2016. The Indo-Pacific Warm Pool: critical to world oceanography and world climate. Geoscience Letters 3, 20. https://doi.org/10.1186/s40562-016-0054-3

De Jonge, C., Hopmans, E.C., Zell, C.I., Kim, J.-H., Schouten, S., Sinninghe Damsté, J.S., 2014. Occurrence and abundance of 6-methyl branched glycerol dialkyl glycerol tetraethers in soils: Implications for palaeoclimate reconstruction. Geochimica et Cosmochimica Acta 141, 97–112. https://doi.org/10.1016/j.gca.2014.06.013

De Jonge, C., Kuramae, E.E., Radujković, D., Weedon, J.T., Janssens, I.A., Peterse, F., 2021. The influence of soil chemistry on branched tetraether lipids in mid- and high latitude soils: Implications for brGDGT- based paleothermometry. Geochimica et Cosmochimica Acta 310, 95–112. https://doi.org/10.1016/j.gca.2021.06.037

Di Nezio, P.N., Timmermann, A., Tierney, J.E., Jin, F., Otto-Bliesner, B., Rosenbloom, N., Mapes, B., Neale, R., Ivanovic, R.F., Montenegro, A., 2016. The climate response of the Indo-Pacific warm pool to glacial sea level. Paleoceanography 31, 866–894. https://doi.org/10.1002/2015PA002890

Diefendorf, A.F., Freimuth, E.J., 2017. Extracting the most from terrestrial plant-derived n-alkyl lipids and their carbon isotopes from the sedimentary record: A review. Organic Geochemistry 103, 1–21. https://doi.org/10.1016/j.orggeochem.2016.10.016

DiNezio, P.N., Tierney, J.E., 2013. The effect of sea level on glacial Indo-Pacific climate. Nature Geosci 6, 485–491. https://doi.org/10.1038/ngeo1823

Douglas, P.M.J., Pagani, M., Brenner, M., Hodell, D.A., Curtis, J.H., 2012. Aridity and vegetation composition are important determinants of leaf-wax δD values in southeastern Mexico and Central America. Geochimica et Cosmochimica Acta 97, 24–45. https://doi.org/10.1016/j.gca.2012.09.005

Dubois, N., Oppo, D.W., Galy, V.V., Mohtadi, M., van der Kaars, S., Tierney, J.E., Rosenthal, Y., Eglinton, T.I., Lückge, A., Linsley, B.K., 2014. Indonesian vegetation response to changes in rainfall seasonality over the past 25,000 years. Nature Geoscience 7, 513–517. https://doi.org/10.1038/ngeo2182

Ehleringer, J.R., Cerling, T.E., Helliker, B.R., 1997. C4 photosynthesis, atmospheric CO2, and climate. Oecologia 112, 285–299. https://doi.org/10.1007/s004420050311

Feakins, S.J., Bentley, L.P., Salinas, N., Shenkin, A., Blonder, B., Goldsmith, G.R., Ponton, C., Arvin, L.J., Wu, M.S., Peters, T., West, A.J., Martin, R.E., Enquist, B.J., Asner, G.P., Malhi, Y., 2016. Plant leaf wax biomarkers capture gradients in hydrogen isotopes of precipitation from the Andes and Amazon. Geochimica et Cosmochimica Acta 182, 155–172. https://doi.org/10.1016/j.gca.2016.03.018

Garcin, Y., Schefuß, E., Schwab, V.F., Garreta, V., Gleixner, G., Vincens, A., Todou, G., Séné, O., Onana, J.-M., Achoundong, G., Sachse, D., 2014. Reconstructing C 3 and C 4 vegetation cover using n -alkane carbon isotope ratios in recent lake sediments from Cameroon, Western Central Africa. Geochimica et Cosmochimica Acta 142, 482–500. https://doi.org/10.1016/j.gca.2014.07.004

Hällberg, P.L., Schenk, F., Yamoah, K.A., Kuang, X., Smittenberg, R.H., 2022. Seasonal aridity in the Indo-Pacific Warm Pool during the Late Glacial driven by El Niño-like conditions. Climate of the Past 18, 1655–1674. https://doi.org/10.5194/cp-18-1655-2022

Hanebuth, T.J.J., Voris, H.K., Yokoyama, Y., Saito, Y., Okuno, J., 2011. Formation and fate of sedimentary depocentres on Southeast Asia's Sunda Shelf over the past sea-level cycle and biogeographic implications. Earth-Science Reviews 104, 92–110. https://doi.org/10.1016/j.earscirev.2010.09.006

Hare, V.J., Loftus, E., Jeffrey, A., Ramsey, C.B., 2018. Atmospheric CO2 effect on stable carbon isotope composition of terrestrial fossil archives. Nature Communications 9. https://doi.org/10.1038/s41467-017-02691-x

Harris, I., Jones, P.D., Osborn, T.J., Lister, D.H., 2014. Updated high-resolution grids of monthly climatic observations – the CRU TS3.10 Dataset. International Journal of Climatology 34, 623–642. https://doi.org/10.1002/joc.3711

Harris, I., Osborn, T.J., Jones, P., Lister, D., 2020. Version 4 of the CRU TS monthly high-resolution gridded multivariate climate dataset. Scientific Data 7, 1–18. https://doi.org/10.1038/s41597-020-0453-3

Heaney, L.R., 1991. A synopsis of climatic and vegetational change in Southeast Asia. Climatic Change 19, 53–61. https://doi.org/10.1007/BF00142213

Hopmans, E.C., Schouten, S., Sinninghe Damsté, J.S., 2016. The effect of improved chromatography on GDGT-based palaeoproxies. Organic Geochemistry 93, 1–6. https://doi.org/10.1016/j.orggeochem.2015.12.006

Jalihal, C., Bosmans, J.H.C., Srinivasan, J., Chakraborty, A., 2019. The response of tropical precipitation to Earth's precession: the role of energy fluxes and vertical stability. Clim. Past 15, 449–462. https://doi.org/10.5194/cp-15-449-2019

Kathayat, G., Cheng, H., Sinha, A., Berkelhammer, M., Zhang, H., Duan, P., Li, H., Li, X., Ning, Y., Edwards, R.L., 2018. Evaluating the timing and structure of the 4.2 ka event in the Indian summer monsoon domain from an annually resolved speleothem record from Northeast India. Climate of the Past 14, 1869–1879. https://doi.org/10.5194/cp-14-1869-2018

Konecky, B., Russell, J., Bijaksana, S., 2016. Glacial aridity in central Indonesia coeval with intensified monsoon circulation. Earth and Planetary Science Letters 437, 15–24. https://doi.org/10.1016/j.epsl.2015.12.037

Koutavas, A., Joanides, S., 2012. El Niño-Southern Oscillation extrema in the Holocene and Last Glacial Maximum: ENSO EXTREMA IN THE HOLOCENE AND LGM. Paleoceanography 27. https://doi.org/10.1029/2012PA002378

Laskar, J., Robutel, P., Joutel, F., Gastineau, M., Correia, A.C.M., Levrard, B., 2004. A long-term numerical solution for the insolation quantities of the Earth. A&A 428, 261–285. https://doi.org/10.1051/0004-6361:20041335

Lewis Jr, W.M., 1996. Tropical lakes: how latitude makes a difference. Perspectives in tropical limnology 4364.

Liu, W., Yang, H., 2008. Multiple controls for the variability of hydrogen isotopic compositions in higher plant *n* -alkanes from modern ecosystems: VARIABILITY OF HYDROGEN ISOTOPIC COMPOSITIONS. Global Change Biology 14, 2166–2177. https://doi.org/10.1111/j.1365-2486.2008.01608.x

Mohtadi, M., Prange, M., Schefuß, E., Jennerjahn, T.C., 2017. Late Holocene slowdown of the Indian Ocean Walker circulation. Nat Commun 8, 1–8. https://doi.org/10.1038/s41467-017-00855-3

Monnin, E., 2006. EPICA Dome C high resolution carbon dioxide concentrations. https://doi.org/10.1594/PANGAEA.472488

Murphy, B.P., Bowman, D.M.J.S., 2007. Seasonal water availability predicts the relative abundance of C_3 and C_4 grasses in Australia. Global Ecol Biogeography 16, 160–169. https://doi.org/10.1111/j.1466-8238.2006.00285.x

Naafs, B.D.A., Inglis, G.N., Zheng, Y., Amesbury, M.J., Biester, H., Bindler, R., Blewett, J., Burrows, M.A., del Castillo Torres, D., Chambers, F.M., Cohen, A.D., Evershed, R.P., Feakins, S.J., Gałka, M., Gallego-Sala, A., Gandois, L., Gray, D.M., Hatcher, P.G., Honorio Coronado, E.N., Hughes, P.D.M., Huguet, A., Könönen, M., Laggoun-Défarge, F., Lähteenoja, O., Lamentowicz, M., Marchant, R., McClymont, E., Pontevedra-Pombal, X., Ponton, C., Pourmand, A., Rizzuti, A.M., Rochefort, L., Schellekens, J., De Vleeschouwer, F., Pancost, R.D., 2017. Introducing global peat-specific temperature and pH calibrations based on brGDGT bacterial lipids. Geochimica et Cosmochimica Acta 208, 285–301. https://doi.org/10.1016/j.gca.2017.01.038

Partin, J.W., Cobb, K.M., Adkins, J.F., Clark, B., Fernandez, D.P., 2007. Millennial-scale trends in west Pacific warm pool hydrology since the Last Glacial Maximum. Nature 449, 452–455. https://doi.org/10.1038/nature06164

Pausata, F.S.R., Battisti, D.S., Nisancioglu, K.H., Bitz, C.M., 2011. Chinese stalagmite δ18O controlled by changes in the Indian monsoon during a simulated Heinrich event. Nature Geosci 4, 474–480. https://doi.org/10.1038/ngeo1169

Pinto, H., Sharwood, R.E., Tissue, D.T., Ghannoum, O., 2014. Photosynthesis of C3, C3–C4, and C4 grasses at glacial CO2. J Exp Bot 65, 3669–3681. https://doi.org/10.1093/jxb/eru155

Porter, S.C., 2000. Snowline depression in the tropics during the Last Glaciation. Quaternary Science Reviews 20, 1067–1091. https://doi.org/10.1016/S0277-3791(00)00178-5

Randerson, J.T., Werf, G.R. van der, Collatz, G.J., Giglio, L., Still, C.J., Kasibhatla, P., Miller, J.B., White, J.W.C., DeFries, R.S., Kasischke, E.S., 2005. Fire emissions from C3 and C4 vegetation and their influence on interannual variability of atmospheric CO2 and δ13CO2. Global Biogeochemical Cycles 19. https://doi.org/10.1029/2004GB002366

Rattray, J.E., Smittenberg, R.H., 2020. Separation of Branched and Isoprenoid Glycerol Dialkyl Glycerol Tetraether (GDGT) Isomers in Peat Soils and Marine Sediments Using Reverse Phase Chromatography. Front. Mar. Sci. 7. https://doi.org/10.3389/fmars.2020.539601

Reimer, P.J., Bard, E., Bayliss, A., Beck, J.W., Blackwell, P.G., Ramsey, C.B., Buck, C.E., Cheng, H., Edwards, R.L., Friedrich, M., Grootes, P.M., Guilderson, T.P., Haflidason, H., Hajdas, I., Hatté, C., Heaton, T.J., Hoffmann, D.L., Hogg, A.G., Hughen, K.A., Kaiser, K.F., Kromer, B., Manning, S.W., Niu, M., Reimer, R.W., Richards, D.A., Scott, E.M., Southon, J.R., Staff, R.A., Turney, C.S.M., Plicht, J. van der, 2013. IntCal13 and Marine13 Radiocarbon Age Calibration Curves 0–50,000 Years cal BP. Radiocarbon 55, 1869–1887. https://doi.org/10.2458/azu_js_rc.55.16947

Russell, J.M., Hopmans, E.C., Loomis, S.E., Liang, J., Damsté, J.S.S., 2018. Distributions of 5-and 6-methyl branched glycerol dialkyl glycerol tetraethers (brGDGTs) in East African lake sediment: Effects of temperature, pH, and new lacustrine paleotemperature calibrations. Organic Geochemistry 117, 56–69.

Russell, J.M., Vogel, H., Konecky, B.L., Bijaksana, S., Huang, Y., Melles, M., Wattrus, N., Costa, K., King, J.W., 2014. Glacial forcing of central Indonesian hydroclimate since 60,000 y B.P. Proceedings of the National Academy of Sciences 111, 5100–5105. https://doi.org/10.1073/pnas.1402373111

S Snansieng, Gitisan, N, Sripongnan, P., 1976. Geological map of Changwat Nakhon Si Thammarat.

Sachse, D., Billault, I., Bowen, G.J., Chikaraishi, Y., Dawson, T.E., Feakins, S.J., Freeman, K.H., Magill, C.R., McInerney, F.A., van der Meer, M.T.J., Polissar, P., Robins, R.J., Sachs, J.P., Schmidt, H.-L., Sessions, A.L., White, J.W.C., West, J.B., Kahmen, A., 2012. Molecular Paleohydrology: Interpreting the Hydrogen-Isotopic Composition of Lipid Biomarkers from Photosynthesizing Organisms. Annu. Rev. Earth Planet. Sci. 40, 221–249. https://doi.org/10.1146/annurev-earth-042711-105535

Sachse, D., Radke, J., Gleixner, G., 2004. Hydrogen isotope ratios of recent lacustrine sedimentary n-alkanes record modern climate variability. Geochimica et Cosmochimica Acta 68, 4877–4889. https://doi.org/10.1016/j.gca.2004.06.004

Schouten, S., Hopmans, E.C., Sinninghe Damsté, J.S., 2013. The organic geochemistry of glycerol dialkyl glycerol tetraether lipids: A review. Organic Geochemistry 54, 19–61. https://doi.org/10.1016/j.orggeochem.2012.09.006

Sessions, A.L., Burgoyne, T.W., Schimmelmann, A., Hayes, J.M., 1999. Fractionation of hydrogen isotopes in lipid biosynthesis. Organic Geochemistry 30, 1193–1200. https://doi.org/10.1016/S0146-6380(99)00094-7

Sinninghe Damsté, J.S., Verschuren, D., Ossebaar, J., Blokker, J., van Houten, R., van der Meer, M.T.J., Plessen, B., Schouten, S., 2011. A 25,000-year record of climate-induced changes in lowland vegetation of eastern equatorial Africa revealed by the stable carbon-isotopic composition of fossil plant leaf waxes. Earth and Planetary Science Letters 302, 236–246. https://doi.org/10.1016/j.epsl.2010.12.025

Sobel, A.H., Maloney, E.D., Bellon, G., Frierson, D.M., 2010. Surface fluxes and tropical intraseasonal variability: A reassessment. Journal of Advances in Modeling Earth Systems 2. https://doi.org/10.3894/JAMES.2010.2.2

Street-Perrott, F.A., 1997. Impact of Lower Atmospheric Carbon Dioxide on Tropical Mountain Ecosystems. Science 278, 1422–1426. https://doi.org/10.1126/science.278.5342.1422

Sun, Q., Chu, G., Liu, M., Xie, M., Li, S., Ling, Y., Wang, X., Shi, L., Jia, G., Lü, H., 2011. Distributions and temperature dependence of branched glycerol dialkyl glycerol tetraethers in recent lacustrine sediments from China and Nepal. Journal of Geophysical Research: Biogeosciences 116. https://doi.org/10.1029/2010JG001365

Sun Xiang Jun, L.X., Sun Xiang Jun, L.X., 2002. Vegetation and Climate on the Sunda Shelf of the South China Sea During the Last Glactiation-Pollen Results from Station 17962. J Integr Plant Biol 44.

Tierney, J.E., deMenocal, P.B., 2013. Abrupt Shifts in Horn of Africa Hydroclimate Since the Last Glacial Maximum. Science 342, 843–846. https://doi.org/10.1126/science.1240411

Tierney, J.E., Zhu, J., King, J., Malevich, S.B., Hakim, G.J., Poulsen, C.J., 2020. Glacial cooling and climate sensitivity revisited. Nature 584, 569–573. https://doi.org/10.1038/s41586-020-2617-x

Timmermann, A., An, S.-I., Kug, J.-S., Jin, F.-F., Cai, W., Capotondi, A., Cobb, K.M., Lengaigne, M., McPhaden, M.J., Stuecker, M.F., Stein, K., Wittenberg, A.T., Yun, K.-S., Bayr, T., Chen, H.-C., Chikamoto, Y., Dewitte, B., Dommenget, D., Grothe, P., Guilyardi, E., Ham, Y.-G., Hayashi, M., Ineson, S., Kang, D., Kim, S., Kim, W., Lee, J.-Y., Li, T., Luo, J.-J., McGregor, S., Planton, Y., Power, S., Rashid, H., Ren, H.-L., Santoso, A., Takahashi, K., Todd, A., Wang, Guomin, Wang, Guojian, Xie, R., Yang, W.-H., Yeh, S.-W., Yoon, J., Zeller, E., Zhang, X., 2018. El Niño–Southern Oscillation complexity. Nature 559, 535–545. https://doi.org/10.1038/s41586-018-0252-6

Waelbroeck, C., Labeyrie, L., Michel, E., Duplessy, J.C., McManus, J.F., Lambeck, K., Balbon, E., Labracherie, M., 2002. Sea-level and deep water temperature changes derived from benthic foraminifera isotopic records. Quaternary Science Reviews, EPILOG 21, 295–305. https://doi.org/10.1016/S0277-3791(01)00101-9

Wang, X., Sun, X., Wang, P., Stattegger, K., 2009. Vegetation on the Sunda Shelf, South China Sea, during the Last Glacial Maximum. Palaeogeography, Palaeoclimatology, Palaeoecology 278, 88–97. https://doi.org/10.1016/j.palaeo.2009.04.008

Wang, Y.V., Larsen, T., Leduc, G., Andersen, N., Blanz, T., Schneider, R.R., 2013. What does leaf wax δD from a mixed C3/C4 vegetation region tell us? Geochimica et Cosmochimica Acta 111, 128–139. https://doi.org/10.1016/j.gca.2012.10.016

Wei, Z., Lee, X., Liu, Z., Seeboonruang, U., Koike, M., Yoshimura, K., 2018. Influences of large-scale convection and moisture source on monthly precipitation isotope ratios observed in Thailand, Southeast Asia. Earth and Planetary Science Letters 488, 181–192. https://doi.org/10.1016/j.epsl.2018.02.015

Weijers, J.W.H., Schouten, S., van den Donker, J.C., Hopmans, E.C., Sinninghe Damsté, J.S., 2007. Environmental controls on bacterial tetraether membrane lipid distribution in soils. Geochimica et Cosmochimica Acta 71, 703–713. https://doi.org/10.1016/j.gca.2006.10.003

Wurster, C.M., Bird, M.I., Bull, I.D., Creed, F., Bryant, C., Dungait, J.A.J., Paz, V., 2010. Forest contraction in north equatorial Southeast Asia during the Last Glacial Period. Proceedings of the National Academy of Sciences 107, 15508–15511. https://doi.org/10.1073/pnas.1005507107

Wurster, C.M., Rifai, H., Zhou, B., Haig, J., Bird, M.I., 2019. Savanna in equatorial Borneo during the late Pleistocene. Sci Rep 9, 1–7. https://doi.org/10.1038/s41598-019-42670-4

Wurtzel, J.B., Abram, N.J., Lewis, S.C., Bajo, P., Hellstrom, J.C., Troitzsch, U., Heslop, D., 2018. Tropical Indo-Pacific hydroclimate response to North Atlantic forcing during the last deglaciation as recorded by a speleothem from Sumatra, Indonesia. Earth and Planetary Science Letters 492, 264–278. https://doi.org/10.1016/j.epsl.2018.04.001

Yamoah, K.A., Callac, N., Chi Fru, E., Wohlfarth, B., Wiech, A., Chabangborn, A., Smittenberg, R.H., 2016. A 150-year record of phytoplankton community succession controlled by hydroclimatic variability in a tropical lake. Biogeosciences 13, 3971–3980. https://doi.org/10.5194/bg-13-3971-2016

Yamoah, K.A., Chabangborn, A., Chawchai, S., Fritz, S., Löwemark, L., Kaboth-Bahr, S., Reimer, P.J., Smittenberg, R.H., Wohlfarth, B., 2021. A muted El Niño-like condition during late MIS 3. Quaternary Science Reviews 254, 106782. https://doi.org/10.1016/j.quascirev.2020.106782

Yang, X., Liu, J., Liang, F., Yuan, D., Yang, Y., Lu, Y., Chen, F., 2014. Holocene stalagmite δ^{18}O records in the East Asian monsoon region and their correlation with those in the Indian monsoon region. The Holocene 24, 1657–1664. https://doi.org/10.1177/0959683614551222

Yuan, X., Kaplan, M.R., Cane, M.A., 2018. The Interconnected Global Climate System—A Review of Tropical–Polar Teleconnections. J. Climate 31, 5765–5792. https://doi.org/10.1175/JCLI-D-16-0637.1

Zhang, Brahim, Li, Zhao, Kathayat, Tian, Baker, Wang, Zhang, Ning, Edwards, Cheng, 2019. The Asian Summer Monsoon: Teleconnections and Forcing Mechanisms—A Review from Chinese Speleothem δ18O Records. Quaternary 2, 26. https://doi.org/10.3390/quat2030026

Zhu, C., Lipp, J.S., Wörmer, L., Becker, K.W., Schröder, J., Hinrichs, K.-U., 2013. Comprehensive glycerol ether lipid fingerprints through a novel reversed phase liquid chromatography–mass spectrometry protocol. Organic Geochemistry 65, 53–62. https://doi.org/10.1016/j.orggeochem.2013.09.012

Supplementary Figures

A 18,000-year Record of Tropical Land Temperature, Convective Activity and Rainfall Seasonality from The Maritime Continent

Rienk H Smittenberg [1*], Kweku A Yamoah [1†], Frederik Schenk [1,2], Akkaneewut Chabangborn [1‡], Sakonvan Chawchai [1‡], Minna Väliranta [3], Barbara Wohlfarth

[1] Department of Geological Sciences and Bolin Centre for Climate Research, Stockholm University, Stockholm, Sweden.

[2] Rossby Centre, Swedish Meteorological and Hydrological Institute, 601 76 Norrköping, Sweden.

[3] Environmental Change Research Unit, Department of Environmental Sciences, University of Helsinki, Finland.

† now at School of Geography, University of Birmingham, Birmingham, UK.

‡ now at Department of Geology, Chulalongkorn University, Bangkok 10330, Thailand.

[*] Corresponding author: rienk.smittenberg@geo.su.se

Figure S1. Age model of Lake Nong Thale Prong. Depth is expressed in meter below lake level.

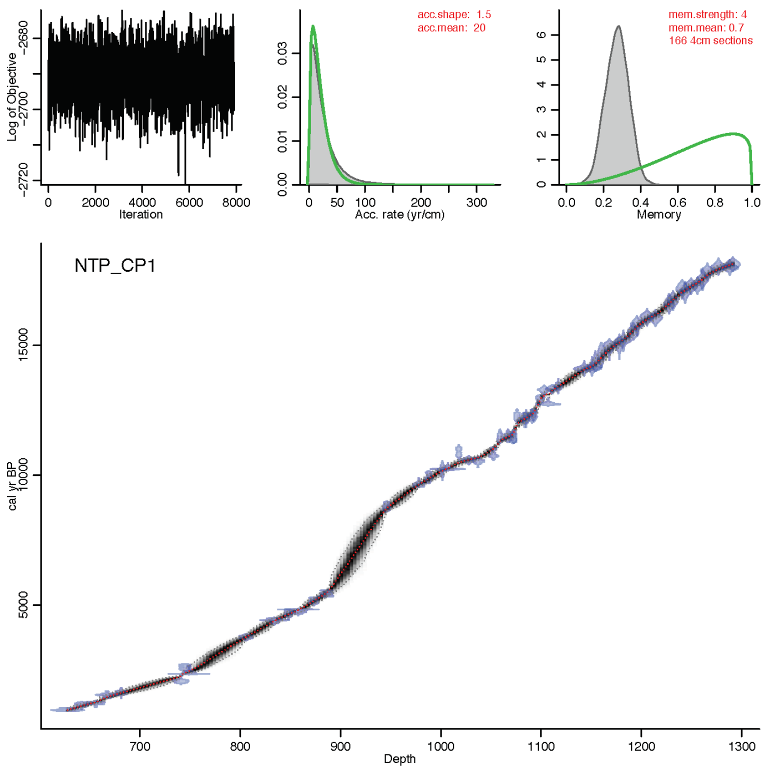

Figure S2. Proxy records of lake Nong Thale Prong, with elements of Fig. 3 in the main paper, extended with TOC content, bulk $\delta^{13}C$, and carbonate content based on loss-on-ignition.

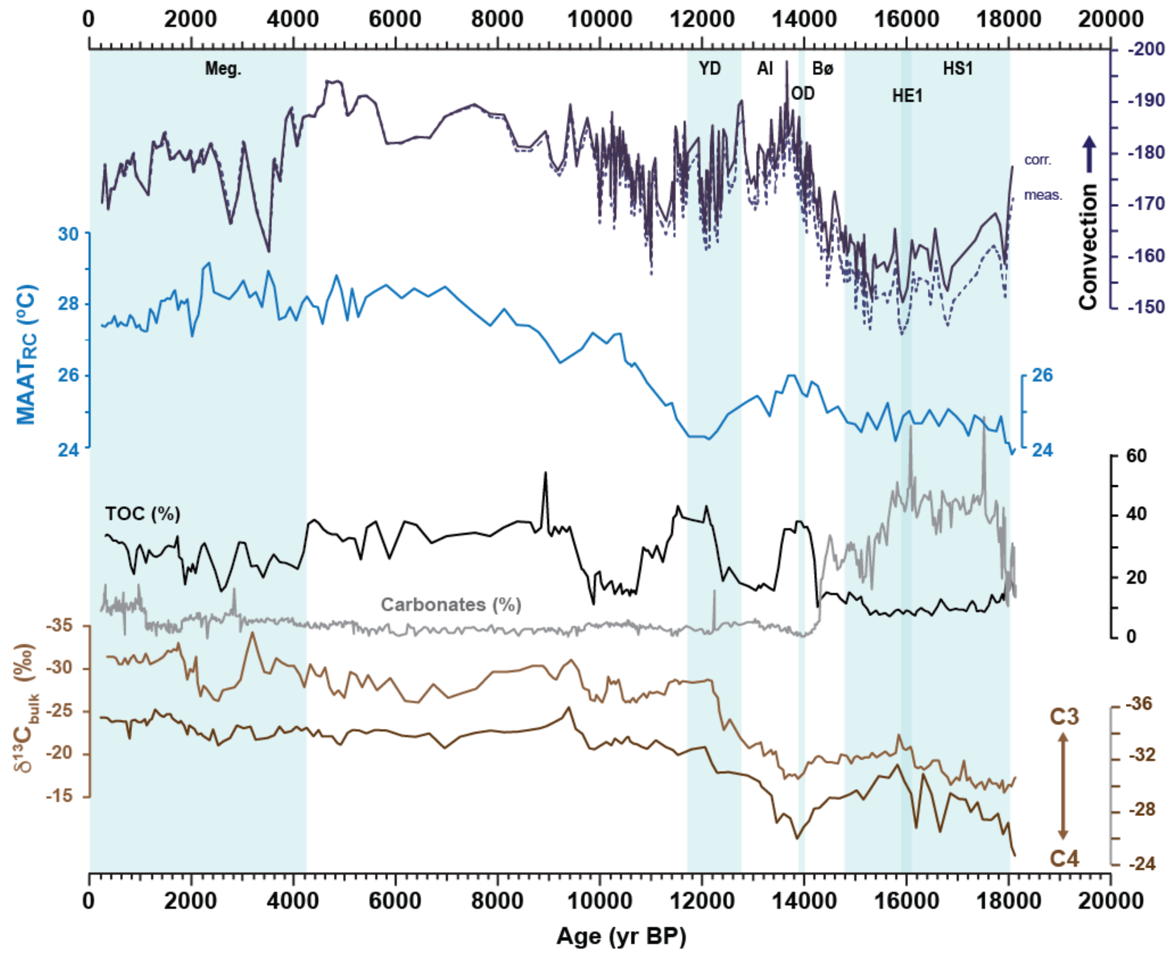

Figure S3. Comparison of the $\delta^{13}C_{wax}$ records of lake NTP (this study) and lake Towuti (Russell et al., 2014) and atmospheric CO_2 levels (Monnin, 2006).

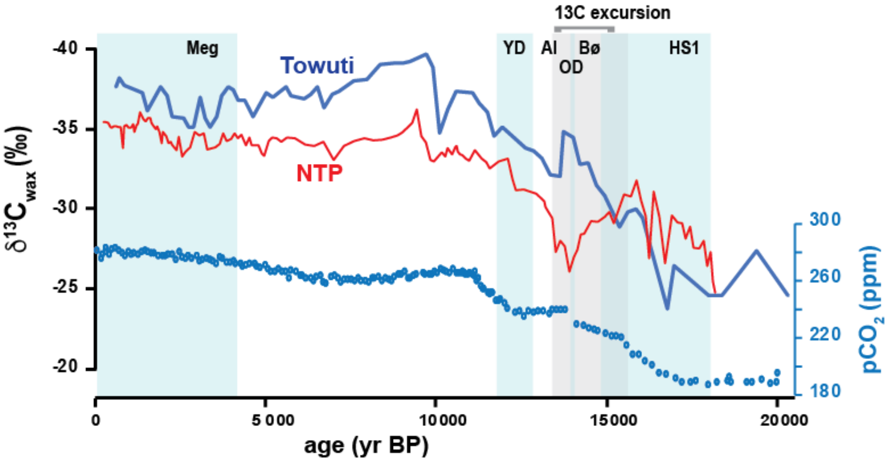

Figure S4. a) Reconstructed MAAT using the MBT/CBT ratios according to two calibrations (Weijers et al., 2007)(Sun et al., 2011), and after local recalibration as described in the text. b) reconstructed pH using the CBT ratios (Weijers et al., 2007)(Sun et al., 2011), c) Triplot of the relative abundance of tetra, penta- and hexamethylated GDGTs in the surface core (green); a the pooled soil and peat (B.D.A. Naafs et al., 2017)(B. D. A. Naafs et al., 2017) (orange) and an African lake dataset (Russell et al., 2018)(light blue) are plotted for reference. d) the same as c, but for the long core NTP data (in red). The reference data set includes both the 5- and 6-methyl GDGTs, while the NTP dataset includes all isomers of the same *m/z*.

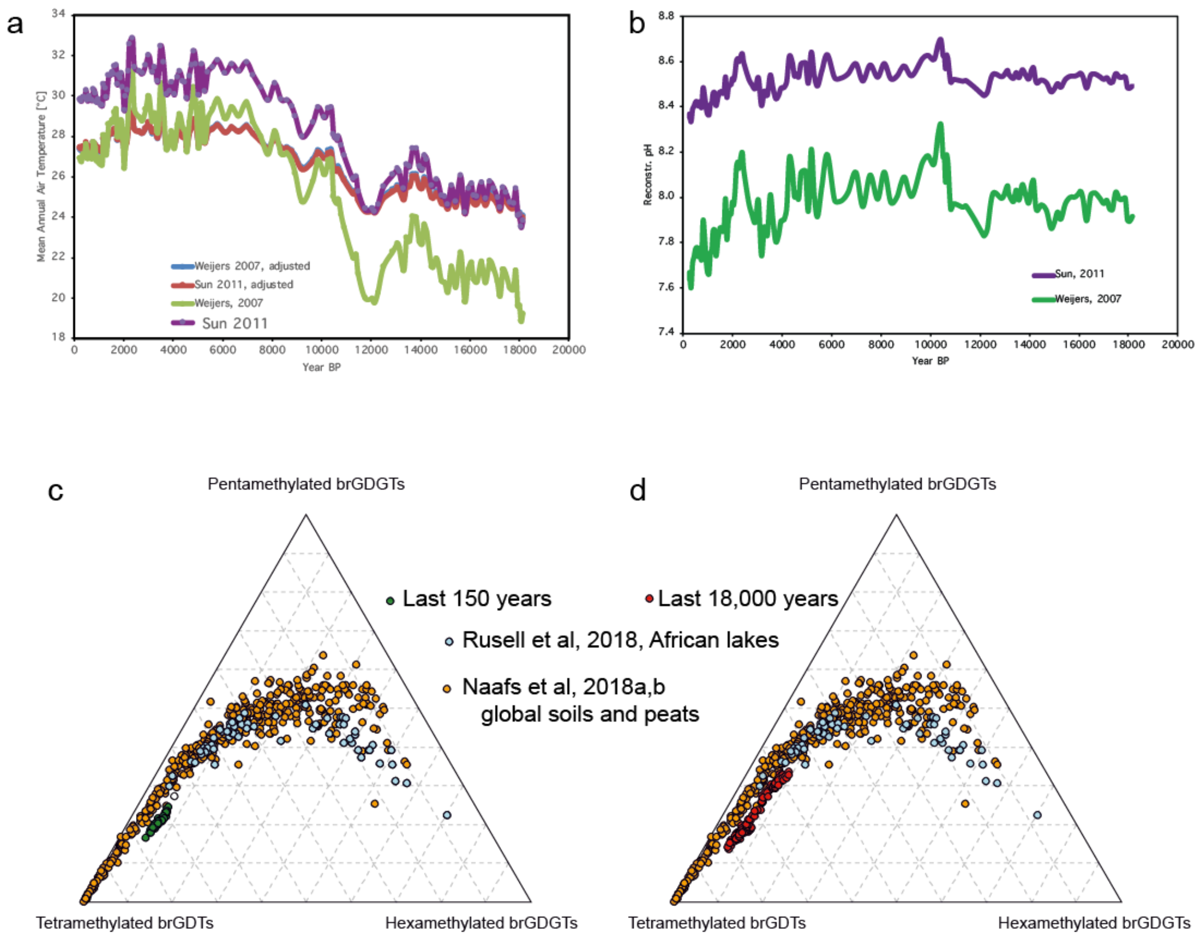

Figure S5. Monthly precipitation of the maritime continent and SE Asia. The wettest months at Lake Nong Thale Prong are associated with the southward passing of the ITCZ from September to November. Maps from http://research.jisao.washington.edu/legates_msu/#analyses (Legates, D. R. and C. J. Willmott, 1990. Mean seasonal and spatial variability in gauge-corrected, global precipitation. Int. J. Climatology, 10, 111-127; Spencer, R. W., 1993: Global oceanic precipitation from the MSU during 1979-91 and comparisons to other climatologies. J. Climate, 6, 1301-1326)

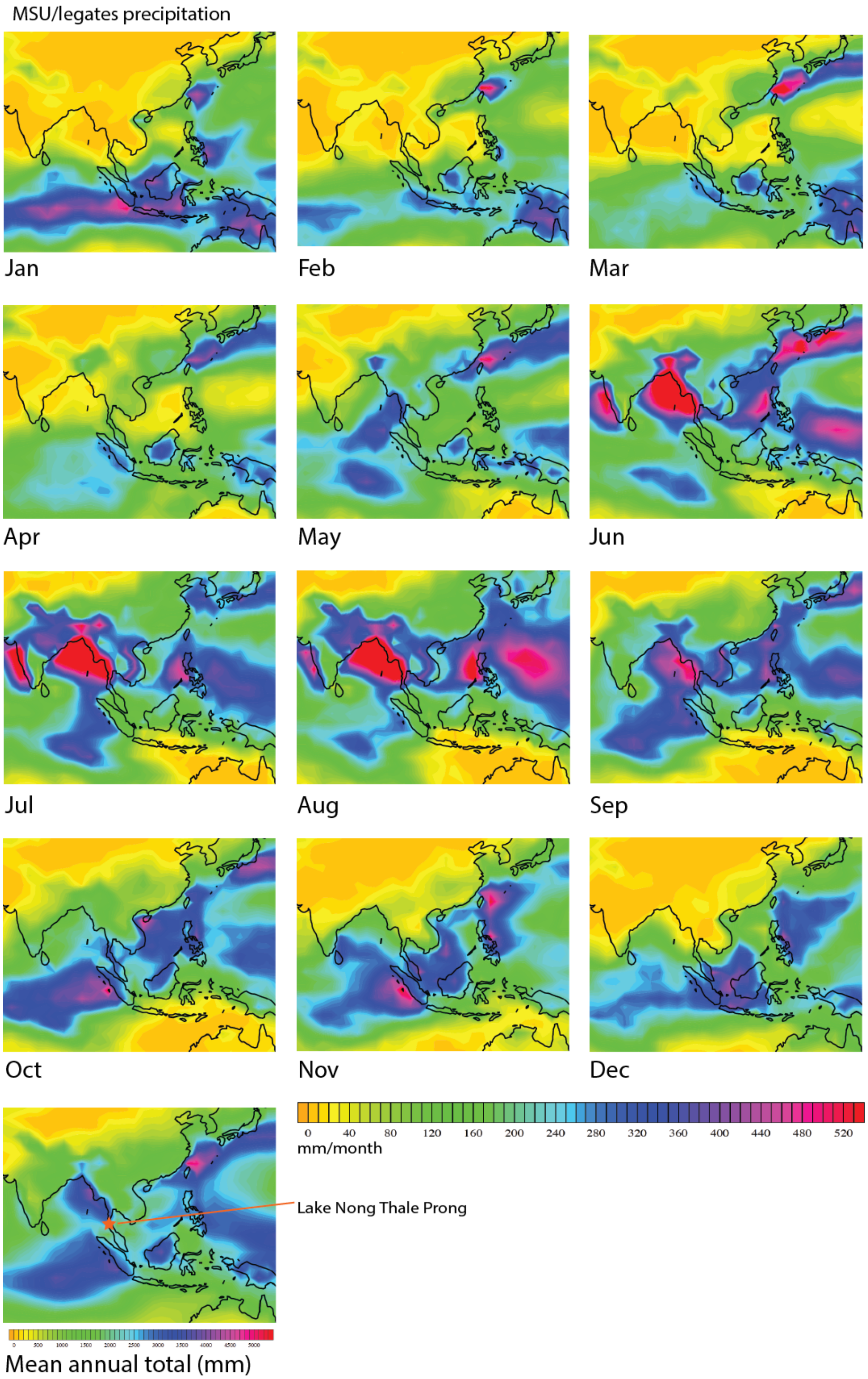

Figure S6. Monthly meteorological data from the two nearest weather stations to lake NTP, Surat Thani (9.12N, 99.35E) and Nakhon Si Thammarat (8.47N, 99.97E), obtained from the Global Historical Climatology Network (GHCN-Monthly) database Version 2. The wettest period is September-November, running even into December (left panels); the warmest months are April-May. Reference: Thomas C. Peterson and Russell S. Vose (1997): Global Historical Climatology Network - Monthly (GHCN-M), Version 2. NOAA National Centers for Environmental Information. doi:10.7289/V5X34VDR [accessed 15 October 2020 using http://climexp.knmi.nl]

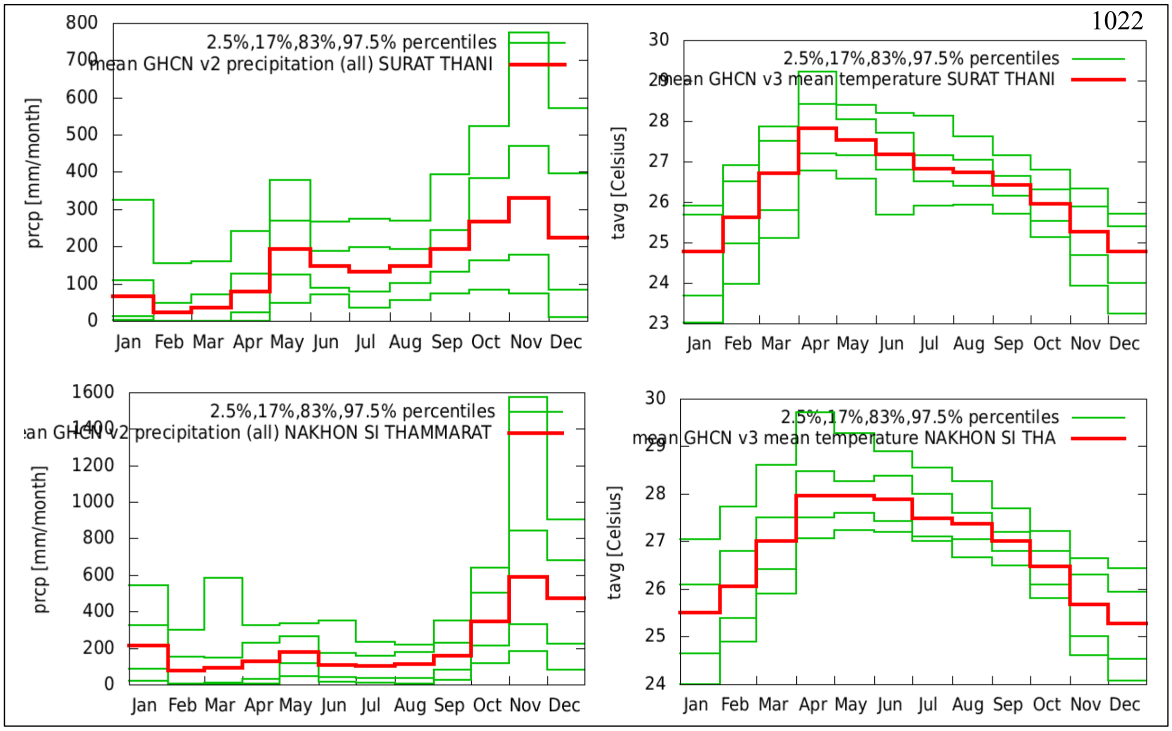

Figure S7. Cross plot of monthly rainfall against monthly insolation for 0° (equator), showing a clear correlation between the two. Rainfall data taken from (Wurtzel et al., 2018) and insolation for the present day (0 ka BP) of Fig. 6 (main text).

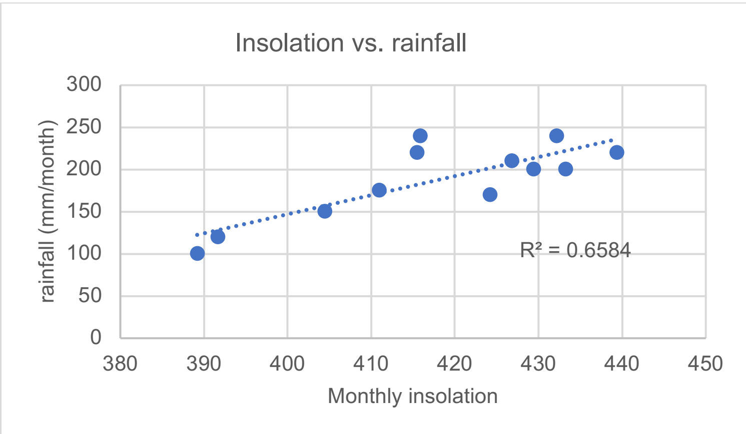

References

Monnin, E., 2006. EPICA Dome C high resolution carbon dioxide concentrations. https://doi.org/10.1594/PANGAEA.472488

Naafs, B. D. A., Gallego-Sala, A.V., Inglis, G.N., Pancost, R.D., 2017. Refining the global branched glycerol dialkyl glycerol tetraether (brGDGT) soil temperature calibration. Organic Geochemistry 106, 48–56. https://doi.org/10.1016/j.orggeochem.2017.01.009

Naafs, B.D.A., Inglis, G.N., Zheng, Y., Amesbury, M.J., Biester, H., Bindler, R., Blewett, J., Burrows, M.A., del Castillo Torres, D., Chambers, F.M., Cohen, A.D., Evershed, R.P., Feakins, S.J., Gałka, M., Gallego-Sala, A., Gandois, L., Gray, D.M., Hatcher, P.G., Honorio Coronado, E.N., Hughes, P.D.M., Huguet, A., Könönen, M., Laggoun-Défarge, F., Lähteenoja, O., Lamentowicz, M., Marchant, R., McClymont, E., Pontevedra-Pombal, X., Ponton, C., Pourmand, A., Rizzuti, A.M., Rochefort, L., Schellekens, J., De Vleeschouwer, F., Pancost, R.D., 2017. Introducing global peat-specific temperature and pH calibrations based on brGDGT bacterial lipids. Geochimica et Cosmochimica Acta 208, 285–301. https://doi.org/10.1016/j.gca.2017.01.038

Russell, J.M., Hopmans, E.C., Loomis, S.E., Liang, J., Damsté, J.S.S., 2018. Distributions of 5-and 6-methyl branched glycerol dialkyl glycerol tetraethers (brGDGTs) in East African lake sediment: Effects of temperature, pH, and new lacustrine paleotemperature calibrations. Organic Geochemistry 117, 56–69.

Russell, J.M., Vogel, H., Konecky, B.L., Bijaksana, S., Huang, Y., Melles, M., Wattrus, N., Costa, K., King, J.W., 2014. Glacial forcing of central Indonesian hydroclimate since 60,000 y B.P. Proceedings of the National Academy of Sciences 111, 5100–5105. https://doi.org/10.1073/pnas.1402373111

Sun, Q., Chu, G., Liu, M., Xie, M., Li, S., Ling, Y., Wang, X., Shi, L., Jia, G., Lü, H., 2011. Distributions and temperature dependence of branched glycerol dialkyl glycerol tetraethers in recent lacustrine sediments from China and Nepal. Journal of Geophysical Research: Biogeosciences 116. https://doi.org/10.1029/2010JG001365

Weijers, J.W.H., Schouten, S., van den Donker, J.C., Hopmans, E.C., Sinninghe Damsté, J.S., 2007. Environmental controls on bacterial tetraether membrane lipid distribution in soils. Geochimica et Cosmochimica Acta 71, 703–713. https://doi.org/10.1016/j.gca.2006.10.003

Wurtzel, J.B., Abram, N.J., Lewis, S.C., Bajo, P., Hellstrom, J.C., Troitzsch, U., Heslop, D., 2018. Tropical Indo-Pacific hydroclimate response to North Atlantic forcing during the last deglaciation as recorded by a speleothem from Sumatra, Indonesia. Earth and Planetary Science Letters 492, 264–278. https://doi.org/10.1016/j.epsl.2018.04.001